Article

On the redox-activity and health-effects of atmospheric primary and secondary aerosol: phenomenology

Francesca Costabile[1*], Stefano Decesari[2], Roberta Vecchi[3], Franco Lucarelli[4,5], Gabriele Curci[6,7], Dario Massabò[8], Matteo Rinaldi[2], Maurizio Gualtieri[9,$], Emanuela Corsini[10], Elena Menegola[11], Silvia Canepari[12], Lorenzo Massimi[12], Stefania Argentini[1], Maurizio Busetto[2], Gianluca Di Iulio[1], Luca Di Liberto[1], Marco Paglione[2], Igor Petenko[1], Mara Russo[2], Angela Marinoni[2], Gianpietro Casasanta[1], Sara Valentini[3], Vera Bernardoni[3], Federica Crova[3], Gianluigi Valli[3], Alice Corina Forello[4], Fabio Giardi[4], Silvia Nava[4,5], Giulia Pazzi[4], Paolo Prati[8], Virginia Vernocchi[8], Teresa La Torretta[9], Ettore Petralia[9], Milena Stracquadanio[9], Gabriele Zanini[9], Gloria Melzi[10], Emma Nozza[3,10], Martina Iulini[10], Donatella Caruso[10], Lucia Cioffi[10], Gabriele Imperato[10], Flavio Giavarini[10], Maria Battistoni[3,11], Francesca Di Renzo[11], Maria Agostina Frezzini[12], Cinzia Perrino[13] and Maria Cristina Facchini[2]

[1] Institute of Atmospheric Sciences and Climate, National Research Council, 00133 Roma, Italy
[2] Institute of Atmospheric Sciences and Climate, National Research Council, 40129 Bologna, Italy
[3] Dept. of Physics, Università degli Studi di Milano, and INFN-Milan, 20133 Milano, Italy
[4] Dept. of Physics and Astronomy, Università degli Studi di Firenze, 50019 Sesto Fiorentino, Italy
[5] National Institute of Nuclear Physics, INFN-Florence, via Sansone 1, 50019 Sesto Fiorentino, Italy
[6] Dept. of physico chemical science, Università degli Studi dell'Aquila, 67100 L'Aquila, Italy
[7] Center of Excellence in Telesensing of Environment and Model Prediction of Severe events (CETEMPS), Università degli Studi dell'Aquila, 67100 L'Aquila, Italy
[8] Dept. of Physics, Università degli Studi di Genova, and INFN-Genoa, 16146 Genova, Italy
[9] ENEA-SSPT-MET-INAT, 40129 Bologna, Italy
[10] Dept. of Pharmacological and Biomolecular Sciences, Università degli Studi di Milano, 20133 Milano, Italy
[11] Dept. of Environmental Science and Policy, Università degli Studi di Milano, 20133 Milano, Italy
[12] Department of Environmental Biology - University of Rome Sapienza, Roma, 00185, Italy
[13] Institute of Air Pollution, National Research Council, Rome, Italy
$ Author present address Department of Earth and Environmental Sciences, University of Milano-Bicocca, 20126 Milano, Italy
* Correspondence: f.costabile@isac.cnr.it; Tel.: +390645488288 .

Abstract: The RHAPS project was launched in 2019 with the major objective to identify specific properties of the fine atmospheric aerosol from combustion sources that are responsible for toxicological effects and can be used as new metrics for health-related outdoor pollution studies. In this paper, we present the overall methodology of RHAPS, and introduce the phenomenology and the first data observed. A comprehensive physico-chemical aerosol characterization has been achieved by means of high-time resolution measurements (e.g. number size distributions, refractory chemical components, elemental composition,) and low-time resolution analyses (e.g. oxidative potential, toxicological assays, chemical composition,…). Preliminary results show a high complexity in the relations observed, the link between air quality and toxicological endpoints being not obvious. We explore data from different points of view: source apportionment of PM_1 and the role of source emissions on aerosol toxicity, the oxidative potential as a predictive variable for PM_1 toxicity with focus on the secondary organic aerosol possessing redox-active capacity, exposure-response relationships for PM_1, and air quality models to forecast PM_1 toxicity. We provide a synthesis of results with the outlook to companion papers where data are analyzed in more detail.

Keywords: atmospheric aerosol; chemical composition; secondary aerosol; source apportionment; ultrafine particles; oxidative potential; exposure; toxicology; forecasting; micrometeorology

1. Introduction

Ambient air pollution is the leading environmental risk factor globally. WHO estimates that exposure to air pollution might be associated with around 7 million deaths,

 doi:10.20944/preprints202204.0107.v1

especially from noncommunicable cardiovascular and respiratory diseases [1] [WHO, 2021]. Among air pollutants, $PM_{2.5}$ (particulate matter with an aerodynamic particle diameter less than 2.5 μm) has received special attention. To date, there is evidence of causal relationships between exposure to $PM_{2.5}$ air pollution and all-cause mortality, as well as several diseases including lung cancer, stroke, respiratory infections, and pulmonary diseases [1, 2, 3] [Cohen et al., 2017; Chen & Hoek, 2020; WHO, 2021]. However, our understanding of this relationship is not clear enough.

WHO in 2021 recommended lowering $PM_{2.5}$ annual air quality guideline level from 10 to 5 μg m^{-3} to reflect the new evidence about effects occurring at low levels of exposure. Indeed, recent outcomes from seven large prospective cohort studies in Europe focusing on low $PM_{2.5}$ concentrations showed positive associations between long-term exposure to low $PM_{2.5}$ and non-accidental, cardiovascular, non-malignant respiratory and lung cancer mortality without an indication of a lower threshold (below 1-5 μg m^{-3}) [4] [Stafoggia et al., 2022]. Among the reasons possibly explaining the occurrence of health effects even at these very low doses, there is the fact that these studies are based on $PM_{2.5}$ mass, a metric that is not ideal in representing the "biologically-active dose" of toxic $PM_{2.5}$. In fact, $PM_{2.5}$ being the same, health impact can significantly vary with the blend of particles and gaseous compounds, as well as additional factors such as mixing, weather, atmospheric chemistry, etc. [5] [Li et al., 2019]. Indeed, $PM_{2.5}$ is characterized by a blend of components, complex mixtures of interacting different types from many emission sources, with physicochemical properties significantly varying in time and space that undergo fast atmospheric transformation processes, and thus may have very diverse toxicological properties. In its 2009 Integrated science assessment for particulate matter, the US Environmental Agency wrote: "there are many components contributing to the health effects of $PM_{2.5}$, but not sufficient evidence to differentiate those constituents (or sources) that are more closely related to specific health outcomes" [6] [EPA, 2009]. Four years later, the REVIHAAP report of the World Health Organization [7] [WHO, 2013], referring to that sentence, wrote: "Despite the increased number of studies (especially epidemiological), after 2009, the general conclusion remains the same in 2013". In 2021, WHO prioritized specific types of PM, i.e., Black Carbon (BC) and Elemental Carbon (EC), Sand and Dust storm particles, and Ultrafine Particles (UFPs) but concluded that the quantitative evidence on independent adverse health effects from these pollutants was still insufficient for new AQG levels [1] [WHO, 2021]. Next to these, a number of studies [8] [Künzi et al., 2015] have highlighted the toxicological potential of secondary organic aerosols (SOA). This discovery demonstrated that ambient aerosols responsible for potential impacts on human health are not only emitted from pollution hotspots. After emission, new toxic compounds can be formed in the atmosphere, the toxicological properties varying as a function of environmental conditions, such as temperature, solar irradiance [9] [Jimenez et al., 2009], and availability of liquid water in form of fog/cloud droplets or deliquesced aerosols [10] [Ervens et al., 2011]. It is worth noting that seasonal differences in toxicological response were observed e.g. in the TOBICUP (TOxicity of BIomass Combustion generated Ultrafine Particles) project when summer vs. winter ambient samples of UFPs were assayed. Indeed, as for UFP summer samples induced more pro-inflammatory response than wintertime ones; opposite, winter UFP samples generated higher genotoxic effects [11, 12, 13] [Corsini et al., 2017a,b; Marabini et al., 2017]. The CARE field study based in Rome during the winter season involved the deployment of a suite of highly time-resolved physical and chemical aerosol characterization along with in-field toxicological measurements [14, 15] [Costabile et al., 2017; Gualtieri et al., 2018]. The results show a complex relationship between $PM_{2.5}$ oxidative and pro-inflammatory properties and primary combustion aerosol concentrations, and indicate that these are greatly impacted by changes in the size and ageing state of the particles in the real atmosphere.

Among the several mechanisms of adverse cellular effects, there are oxygen-free radical-generating activity, DNA oxidative damage, mutagenicity, and stimulation of proinflammatory factors, and the generation of reactive oxygen species (ROS). These

 doi:10.20944/preprints202204.0107.v1

received considerable attention by aerosol scientists, who found in ROS studies an opportunity to link aerosol composition to biological effects [16] [Kelly and Fussell, 2012.]. Best candidates for particulate compounds responsible for ROS activity encompass transition metals and specific organic compounds such as quinoid species [16] [Kelly and Fussell 2012]. Wide ranges of fuels and experimental conditions have been explored in the laboratory to assess the characteristics of combustion aerosols in terms of toxicological endpoints and mechanisms of action (e.g., ROS formation). According to [17] Lakey et al. [2016], the ROS activity of ambient aerosol is a broad function of the logarithm of PM concentrations with a tendency to level off at very high pollution levels. Other authors [18] [Saffari et al. [2014], comparing ROS assays performed on size-segregated PM samples from six cities in three continents, showed that finer aerosol size fractions tend to have a higher ROS activity and that chemical components determining ROS formation include several transition metals and polar organic compounds. Another experiment based in the Po Valley in wintertime showed that fog droplets exhibit a higher intrinsic ROS content with respect to the aerosol particles the fog is formed upon [19] [Decesari et al., 2017], indicating that aqueous-phase reactions in deliquesced particles contribute to alter (possibly amplify) the oxidative potential of PM. The role of PM-induced ROS in lung dysfunction and potential adverse cardiovascular outcomes [20] [Limón-Pacheco et al. 2009] set the basis for the development of chemical (a-cellular) assays suitable for low-cost, widespread observations of ROS formation in ambient PM samples [21] [Ayres et al., 2008]. Their use is considerably extending the data availability for proxies of ambient PM toxicity (linked to oxidative potential) in a variety of environments and for diverse source-related PM fractions [e.g., 22] [Verma et al. 2015]. The results of such studies suggest that atmospheric processing exert a great impact on a parameter, the PM oxidative potential (OP), defined by the ability of aerosol particles to oxidize target (bio)molecules [23] [Borm et al., 2007]. The OP has been tested as an alternative air quality metrics in a few pilot studies [24] [Janssen et al., 2014] but it remains an object of intense research and discussion.

This is the context where the RHAPS (Redox-Activity And Health-Effects Of Atmospheric Primary And Secondary Aerosol) project was launched, in 2019. The major objective of RHAPS is to identify specific properties (or combinations of them) of PM_1 (particles with aerodynamic diameter less than 1 μm) from combustion sources that are responsible for toxicological effects and can be used as new metrics for health-related outdoor pollution studies (Figure 1). By explicitly accounting for atmospheric transport and reactivity, and using experimental and modeling tools, RHAPS aims at providing a new assessment of the sources and nature of PM_1 components responsible for adverse health effects in real-world conditions. The contributions of sub-micron sized chemical components directly emitted in the atmosphere ("primary" aerosols) or formed in-situ by chemical reactions ("secondary" aerosols) on the OP of PM_1 are assessed. In turn, the effect of OP and other PM_1 physical-chemical properties (in particular, size-distributions, water solubility, particle mass/number/surface, composition, etc.) on toxicological endpoints (both in-vitro, such as oxidative stress, inflammation, DNA damage, and in alternative animal models) are investigated. Field campaigns and laboratory experiments in an atmospheric simulation chamber are carried out, the focus on finding a link between the OP carried by SOA and PM_1 toxicity. More specifically, RHAPS has four distinct and specific objectives. Firstly, to apportion sources of PM_1 toxicity and assess relevant processes governing its variability in the atmosphere: primary aerosols (such as fresh traffic and biomass burning), and atmospheric processing (e.g., secondary aerosols, photochemistry, and atmospheric dynamics). Secondly, to characterize the PM_1 fraction possessing redox-active capacity (OP) that is not emitted but formed in the atmosphere upon ageing of the emissions (i.e. the secondary organic aerosol, SOA), through focused lab experiments (ChAMBre) and through comparison with field measurements in tandem monitoring sites (urban background vs. rural) configuration in the Po valley, a known pollution hotspot area in Europe. Thirdly, to assess PM_1 exposure-response relationships (as a function of PM_1 doses, and OP loadings), following a critical assessment of: (i)

Preprints (www.preprints.org) | NOT PEER-REVIEWED | Posted: 12 April 2022 doi:10.20944/preprints202204.0107.v1

predictive capacity of different PM_1 physical-chemical properties (BC, SOA, POA, size, surface area, solubility, particle mass/number/surface, metals, etc.), and (ii) toxicological end-points obtained both in vitro (oxidative stress and inflammation, DNA damage) and in-vivo (embryotoxicity). Finally, to implement air quality models to forecast PM toxicity, by explicitly simulating PM_1 OP, over the investigated area, the entire Po Valley, and the Italian territory.

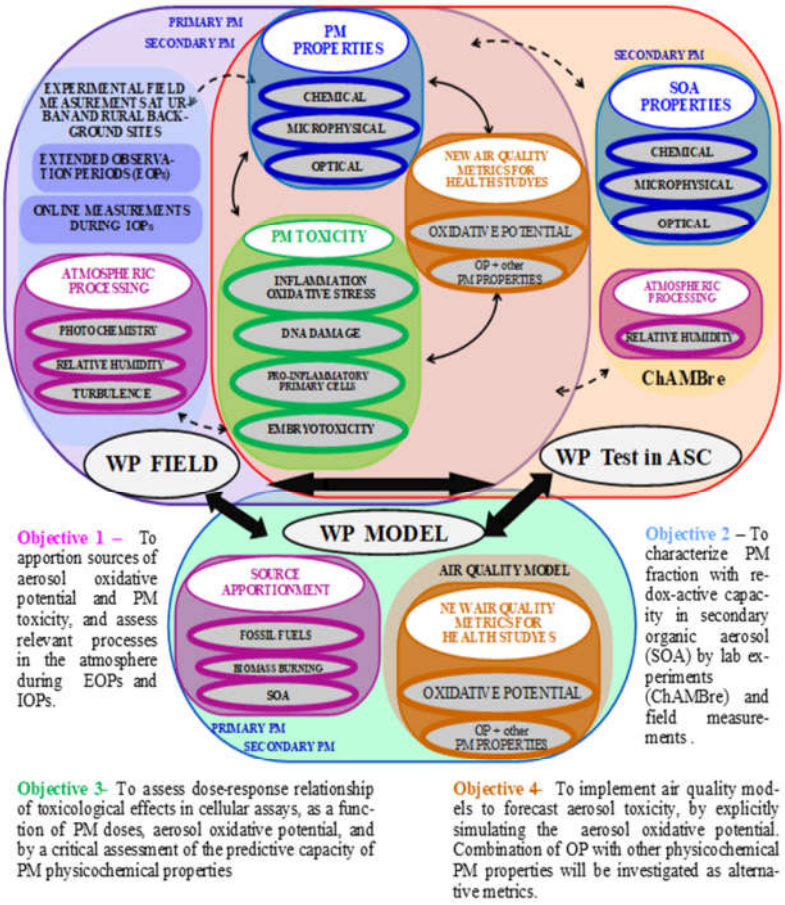

Figure 1. Sketch of the RHAPS project, showing WP and objectives.

In this paper, we present the overall methodology of the RHAPS project, and introduce the phenomenology and the first data observed, which will be discussed in detail in a series of companion papers.

2. Materials and Methods

2.1. Measurement Site

Field observations were carried out in the Po Valley (Italy) using a tandem urban - rural sites combination: BO, urban background, 44°31'29" N, 11°20'27" E) and San Pietro Capo Fiume (SPC, rural, 44°39'15" N, 11°37'29" E). Two reasons provide motivation for a focus on the Po basin during RHAPS: 1) it is one of the major air pollution hotspots in Europe; 2) it provides opportunities to investigate the processes regulating aerosol formation and redox activity in a polluted regional background atmosphere. In the rural

Preprints (www.preprints.org) | NOT PEER-REVIEWED | Posted: 12 April 2022 doi:10.20944/preprints202204.0107.v1

Po Valley, aerosols are mainly emitted from residential wood burning, and also formed in situ by secondary reactions involving ammonia (from agricultural emissions) and the photochemical products of NOx and VOCs (nitric acid and SOA, respectively).

Considering that PM_1-to-$PM_{2.5}$ average ratios in the investigated area was estimated in 60-80 % with lower values in summer vs. winter [25, 26] [Sarti et al., 2015; Vecchi et al., 2004], it is interesting to note that the contribution of secondary sources in the regional background to $PM_{2.5}$ concentrations in the Po Valley vary between 50% (in the largest city, Milan [27] [Amato et al., 2016]) to more than 70% in district cities and rural background sites [28, 29] [Gilardoni et al., 2016; Ricciardelli et al., 2017.]. The effect of the oxidative potential of SOA on the toxicological properties of the Po Valley aerosol is still poorly characterized. We demonstrated, however, that the concentration of the markers of oxidative stress in PM_1 in the rural Po Valley can be of the same order of magnitude of the concentrations reported for US megacities (Los Angeles) [19] [Decesari et al., 2017]. In the same area, fog water, which is enriched of SOA and depleted of transition metals with respect to the aerosol, showed the highest intrinsic redox activity. It is noteworthy that in summer, field measurements were run only at the background urban site, as the atmospheric mixing during the warm season is such that differences between the two sites are largely reduced.

2.2. Obeservational Periods

Given the complexity of the phenomena to observe, we elaborated a field measurement strategy combining different periods, combining intensive and super intensive observational periods (Table 1).

Table 1. Intensive and Super Intensive Observational Periods (IOPs, SIOPs) during RHAPS.

ID	Winter	Summer
IOPs	21/01-18/03 2021	08/06-14/07 2021
SIOPs	26/01-30/01 2021 02/02-06/02 2021 16/02-20/02 2021	29/06-03/07 2021

During Intensive Observational Periods (IOPs) both daily measurements (from h 8.00 a.m. to h 8.00 a.m. local time, ca. 60 samples in winter and 35 in summer) and online and high-time resolution instrumentations were operated in parallel. In winter, IOP was conducted from 21 January to 18 March 2021, and in summer from 8 June to 14 July 2021.

Four super Intensive Observational Periods (SIOPs) were carried out during the project, each SIOP lasting four days (from h 8.00 a.m. to h 8.00 a.m. local time): three SIOPs were carried out in winter (January /February 2021), and one SIOP in summer (June/July 2021). The periods for the SIOPs were planned according to a proper strategy. First, to catch the accumulation of aerosols in the atmosphere, we aimed at having each SIOP lasting four consecutive "stable weather" days, starting from a "clean" day, i.e. good weather possibly following bad weather conditions. Second, to be consistent with emission source paths, we always started the SIOP on Tuesdays and ended on Saturdays. Finally, we aimed at having SIOPs days representative of four source-specific aerosol types: biomass burning (BB), urban aerosol (i.e., traffic emissions), secondary aerosols, and clean conditions. To proxy these aerosols, we selected a subset of variables as described in Table 2. The latter were selected according to our experience and knowledge of the measurement sites, and the analysis of available experimental data obtained during the first part of the IOPs (i.e., PM_1 chemical components, particle number size distribution and BC). Every week, we run a proper air quality model (described in Sect. 2.8) to forecast weather conditions and these variables for the next week, and accordingly we started (or not) the SIOP.

 doi:10.20944/preprints202204.0107.v1

Preprints (www.preprints.org) | NOT PEER-REVIEWED | Posted: 12 April 2022 doi:10.20944/preprints202204.0107.v1

Table 2. exemplary of variables used to identify source-specific aerosol types.

Variables	Urban	BB	SOA/SIA	Clean
BC-to-PM1	↑		↓	
BC-to-OA	↑	↓	↓	
AAE (467-660)	↓	↑		
Nitrate mass concentration			↑	↓
Sulfate mass concentration			↑	↓
Primary OC mass concentration	↑	↑		
Secondary OC mass concentration			↑	
Median particle diameter	↓	↓	↑	
PM1 mass concentration			↑	↓
BC mass concentration	↓	↑		↓
Number concentration	↑			↓
Secondary formaldehyde			↑	
Weather conditions	stable	stable	Stable, foggy	Strong winds, low pressure, no rain

2.3. Aerosol Measurements

2.3.1. PM_1 mass and chemical composition - Daily samples characterization

At both sites many parallel sampling lines were deployed to collect samples devoted to a comprehensive aerosol chemical characterization in terms of mass concentration, elements, ions, and carbonaceous components (PAHs included), to OP assessment, and to toxicological assays (see Table 3 for a summary). PM_1 daily samples were collected on PTFE filters (Pall R2PJ047) and on pre-fired 47 mm diameter quartz-fiber filters (Pallflex Tissuquartz 2500 QAO-UP) according to the specific analysis foreseen for that sample as reported in Table 3. A total of 813 daily samples were collected in winter and 234 in summer.

Table 3. summary of sampling lines and filters used.

WINTER CAMPAIGN (21/01/2021 – 18/03/2021)					
Urban background site (BO)					
Sampler	**Flowrate**	**Inlet**	**Sampling time**	Filters	Target
Dual channel (Dadolab Gemini)	1.15 m^3/h	Modified PM1	24h from 8:00 to 08:00 LT	Quartz-fibre PTFE	Ions (by IC), levoglucosan (HPAEC-PAD) Elements (PIXE)
Dual channel (Dadolab Gemini)	1.15 m^3/h	Modified PM1	24h from 8:00 to 08:00 LT	2 PTFE	Toxicological assays and embryotoxicity
Single channel (Dadolab Giano)	1.15 m^3/h	Modified PM1	24h from 8:00 to 08:00 LT	PTFE	Water soluble oxidative potential
Single channel (Dadolab Giano)	1.15 m^3/h	Modified PM1	24h from 8:00 to 08:00 LT	PTFE	Trace metals (ICP-MS)
Single channel (TCR-Tecora Skypost)	1.15 m^3/h	Modified PM1	24h from 8:00 to 08:00 LT	Quartz fibre	Oxidative potential – OP tot
STRAS	0.5 m^3/h	Modified PM1	1h	Polycarbonate	1h resolved elements (PIXE)
Single channel (TCR-Tecora Skypost)	2.3 m^3/h	PM1	48h from 8:00 to 08:00 LT	Pre-fired quartz fibre	^{14}C

Preprints (www.preprints.org) | NOT PEER-REVIEWED | Posted: 12 April 2022 doi:10.20944/preprints202204.0107.v1

HV sampler (TCR-Tecora)	30 m^3/h	PM1	24h from 8:00 to 08:00 LT	Quartz fibre	Extra analyses
Rural background site (SPC)					
Dual channel (Dadolab Gemini)	1.15 m^3/h	Modified PM1	24h from 8:00 to 08:00 LT	Quartz-fibre PTFE	Ions (by IC), levoglucosan (HPAEC-PAD) Elements (PIXE)
Dual channel (Dadolab Gemini)	1.15 m^3/h	Modified PM1	24h from 8:00 to 08:00 LT	2 PTFE	Toxicological assays and embryotoxicity
Dual channel (Dadolab Gemini)	1.15 m^3/h	Modified PM1	24h from 8:00 to 08:00 LT	2 PTFE	Water soluble oxidative potential Trace metals (ICP-MS)
Single channel (TCR-Tecora Skypost)	1.15 m^3/h	Modified PM1	24h from 8:00 to 08:00 LT	Quartz fibre	Oxidative potential – OP tot
STRAS	0.5 m^3/h	Modified PM1	1h	Polycarbonate	1h resolved elements (PIXE)
SUMMER CAMPAIGN (08/06/2021 – 14/07/2021)					
Urban background site (BO)					
Dual channel (Dadolab Gemini)	2.3 m^3/h	PM1	24h from 8:00 to 08:00 LT	Quartz-fibre PTFE	Ions (by IC), levoglucosan (HPAEC-PAD) Elements (PIXE)
Dual channel (Dadolab Gemini)	2.3 m^3/h	PM1	24h from 8:00 to 08:00 LT	2 PTFE	Toxicological assays and embryotoxicity
Dual channel (Dadolab Gemini)	2.3 m^3/h	PM1	24h from 8:00 to 08:00 LT	2 PTFE	Water soluble oxidative potential Trace metals (ICP-MS)
STRAS	0.5 m^3/h	Modified PM1	2h	Polycarbonate	2h resolved elements (PIXE)
Single channel (Dadolab Giano)	2.3 m^3/h	PM1	24h from 8:00 to 08:00 LT	Quartz fibre	Oxidative potential – OP tot
Single channel (TCR-Tecora Skypost)	2.3 m^3/h	PM1	72h from 8:00 to 08:00 LT	Pre-fired quartz fibre	^{14}C
HV sampler (TCR-Tecora)	30 m^3/h	PM1	24h from 8:00 to 08:00 LT	Quartz fibre	Extra analyses

The low-volume samplers - many of them provided of 2 parallel sampling lines - were operated at 1.15 m^3/h during the winter campaign in order to avoid filter clogging and high pressure drops. To this aim, the sampling inlets were modified by plugging 8 out of 16 nozzles; opposite, the flowrate during the summer campaign was set at 2.3 m^3/h and no modifications to the standard 16 nozzles PM_1 inlet were done. An identical sampling configuration was adopted at both sites.

Mass concentration was gravimetrically determined on PTFE filters using a Sartorius microbalance with 1 μg sensitivity and equipped with an automatic sample changer.

PTFE filters were analyzed by PIXE analysis at the INFN-LABEC accelerator facility in Florence to obtain the elemental concentration of Z>10 elements [30] (Lucarelli, 2020) and by ICP-MS (Bruker 820-MS, Billerica, MA, USA) at Sapienza University of Rome to retrieve the soluble and/or insoluble fraction of Al, As, Ba , Bi , Cd, Ce, Co, Cr, Cs, Cu, Fe, Ga, K, La, Li, Mn, Mo, Na, Pb, Rb, Sb, Sn, Ti, Tl, U, V, W, Zn, and Zr by applying a chemical fractionation procedure that increases the selectivity of the elements as source tracers [31]

 doi:10.20944/preprints202204.0107.v1

[Massimi et al., 2020a]. Instrumental conditions and performance of the method are described in [32, 33] [Astolfi et al. (2020) and Canepari et al. (2009)], respectively.

Punches from quartz-fiber filters were analyzed at the University of Genoa with Ion Chromatography analysis for major ions (Cl^-, NO_3^-, SO_4^{2-}, Na^+, NH_4^+, K^+, Mg^{2+}, Ca^{2+}) [34] [Piazzalunga et al., 2013] and for levoglucosan (1,6-Anhydro-beta-glucopyranose) with HPLC-PAD following [35] [Piazzalunga et al., 2010]. Further details are reported in the Supplementary material.

Elemental and organic carbon fractions (EC and OC) were determined on one punch taken from 24-h quartz-fiber filters by thermo-optical analysis with an offline OCEC Carbon Aerosol Analyser (Sunset Laboratory Inc.,) by applying the NIOSH-QUARTZ temperature protocol.

PAHs - i.e. benzo(α)anthracene, chrysene, benzo(β)fluoranthene and benzo(α)pyrene - were also evaluated in samples collected on quartz filters. The samples were prepared according to previous works [36, 37] [Terzopoulou et al., 2015; Gosetti et al., 2011] with some modifications. For the quantitative analysis benz(α)anthracene-D12 was added as internal standard (200 ng/sample) to all filters. The quantitative analysis was performed using gas chromatography (Varian 3900 GC) supplied by ion trap mass spectrometry (Varian Saturn 2100T). The chromatographic separation was achieved with TG-5SILMS column. Further details can be found in the Supplementary Material.

2.3.2. Non-Refractory PM_1 Chemical Components (AMS)

The mass loading and chemical composition of submicron aerosol particles were obtained online by the High-Resolution Time-of-Flight Aerosol Mass Spectrometer (HR-TOF-AMS, Aerodyne Research) [38] (Canagaratna et al. 2007) at both locations. The HR-TOF-AMS provides measurements of the non-refractory sulfate, nitrate, ammonium, chloride, and organic mass of the submicron particles (NR-PM_1). The working principle of the HR-TOF-AMS is described in detail in [38, 39, 40] [Canagaratna et al. (2007), Jayne et al. (2000), and Jimenez et al. (2003)]. Briefly, during all the campaigns, the HR-TOF-AMS was operating in "V" ion path modes every 2.5 min. The resolving power [41] (DeCarlo et al., 2006) of the V-ion mode was about 2000-2200 during all the campaigns.

Ionization efficiency (IE) calibrations were performed before and after every campaign, and approximately once every two weeks during the campaigns. Filter blank acquisitions during the campaign were performed at least once a day to evaluate the background and correct for the gas-phase contribution. All data were analyzed using the standard ToF-AMS analysis software SQUIRREL v1.57 and PIKA v1.16 (D. Sueper, available at: http://cires.colorado.edu/jimenez-group/ToFAMSResources/ToFSoftware/index.html) within Igor Pro 6.2.1 (WaveMetrics, Lake Oswego, OR). The HR-TOF-AMS collection efficiency (CE) was calculated based on aerosol composition, according to Middlebrook et al. (2012) and confirmed against parallel offline measurements. At both sampling stations, the aerosol was dried to about 35-40% by means of a Nafion drier before sampling with the HR-TOF-AMS.

2.3.3. Elemental composition (STRAS)

High-time resolution samples have been collected at both BO and SPC using the STRAS sampler (Size and Time Resolved Aerosol Sampler), which has been recently developed as an upgrade of the previous streaker sampler to collect the aerosol fine and coarse fractions with high-time resolution. In RHAPS a PM_1 inlet was mounted on STRAS and the particles were sampled with 1-h resolution during winter (for a total of 2352 time slots) and 2-h resolution during summer (for a total of 401 time slots) on a polycarbonate filter; each filter collects up to 168 samples corresponding to 1 week of hourly samples.

STRAS spots were analyzed by PIXE at the INFN-LABEC for off-line high throughput determination of elements with Z>10 [42] [Calzolai et al., 2015].

2.3.4. Particle Number size distributions

 doi:10.20944/preprints202204.0107.v1

The Particle number size distribution (PNSD) was measured at the urban background site of BO by combining a Mobility Particle Size Spectrometer (TROPOS SMPS) equipped with a butanol-based condensation particle counter (CPC, TSI model 3772) and a commercial aerodynamic particle sizer (APS, TSI). Particles from 8 to 800 nm of electrical mobility diameter (d_m) were sized and counted by the SMPS; particles from 0.5 to 20 μm of aerodynamic diameter (d_a) were sized and counted by the APS. SMPS data were corrected for penetration errors through the sampling line (TROPOS-made software), penetration efficiency due to diffusion losses (calculated according to [43] [Hinds, 1999]) being higher than 98.92% for particles bigger than 15 nm. The aerosol sampling line was dried down to relative humidity of about 30% by means of a Nafion drier.

PM1 mass concentration with 5 minute time resolution was constructed from the PNSD data, according to the procedure described elsewhere [Costabile et al., 2017]. In short, PM1 was calculated from the particle volume size distribution under the hypothesis of spherical particles, and a size-dependent particle density varying from 1.25 to 1.5 g cm^{-3} . The daily PM1 from SMPS was then validated according to the daily PM1 measured through the reference procedure, the goodness of fit (R^2=0.99) being presented in the Supplementary Material.

2.3.5. Absorption and scattering coefficients (Aethalometer, PAX, DBAP, filters)

An optical characterization of the daily samples collected at both sites on quartz-fiber filters was performed by Multi Wavelength Absorption Analyzer [44, 45] [Massabò et al., 2013 and 2015] to retrieve the absorption coefficients at five different wavelengths (λ = 850, 635, 532, 405, and 375 nm). A blank filter was used as reference for both winter and summer samples analysis.

In addition to the determination of Ångström Absorption Exponent (AAE) [46] (Moosmüller et al., 2011), previous research studies showed that multi-wavelength absorption coefficients were proved to be effective for apportioning contributions from fossil fuels and biomass burning combustion sources in aerosol samples [e.g., [45, 47] [Sandradewi et al., 2008; Massabò et al., 2015]. The determined absorption coefficients were apportioned following the methodology presented in [45, 48] (Massabò et al., 2015; Bernardoni et al., 2017) and as previously employed in several field campaigns at urban and rural sites [49, 50] [Massabò et al, 2019 and 2020]. The methodology differentiates and quantify the contribution to total absorption of equivalent black carbon (eBC) emitted by wood burning (eBC_{WB}) and fossil fuel (eBC_{FF}) as well as brown carbon (BrC) due to incomplete combustion.

During the winter campaign, two photoacoustic extinction-meters (PAXs, Droplet Measurement Technologies, Boulder, CO, USA) provided the online determination of PM10 absorption and scattering coefficients at λ = 532 and 405 nm, with 1-minute resolution.

At the background urban site of Bologna, a 7-wavelength (370, 470, 520, 590, 660, 880 and 950 nm) aethalometer (model A33, Magee scientific [51] [Drinovec et al., 2015]) provided eBC mass concentration and AAE with 1-min time resolution. According to the instrument manufacturer, the eBC mass concentration from AE33 was obtained from measurements at λ = 880 nm, with a mass absorption coefficient of 7.77 m^2 g^{-1} [51] [Drinovec et al., 2015]. The aerosol sampling line was dried to about 20-30% by means of a Nafion drier.

At the rural site of SPC a Dual Beam Absorption Photometer (DBAP) was used. DBAP5 is a 5 wavelength (from 420 to 870 nm) filter absorption photometer based on the dual beam technology that measures the absorption properties of the particulate matter. Starting from the measurement of the filter light transmission variation over time due to the particle load, it evaluates the attenuation coefficients, then, applying the appropriate filter correction equations, the absorption coefficient and the Equivalent Black Carbon concentration using the Mass Absorption Coefficients. The dual beam technology is a

 doi:10.20944/preprints202204.0107.v1

technique that simultaneously compare the absorption of the particulate matter with the absorption on the white filter, providing more precise measurement especially in low concentration sites.

2.3.6. EC and OC - online measurements

The EC and OC mass concentration with 2-h time resolution was obtained by a Sunset Field Thermal-Optical Analyzer (Model-4 Semi-Continuous OC-EC Field Analyzer – Sunset Laboratory inc.).

Briefly, this instrument collects PM on a quartz fiber filter and automatically analyses it at the end of each sampling period. The instrument inlet is equipped with a cyclone (cut point 1 μm) and a denuder for organics. In this campaign, a time resolution of 2-h (105 min of sampling followed by 15 min of analysis) was chosen as a compromise to get an adequate time resolution (comparable with that of other instruments used in this project) and a sufficient amount of collected sample mass (to maintain a good accuracy in the EC and OC quantification). The instrument was calibrated by sucrose standards and the NIOSH protocol was used for thermal analysis.

Elemental and organic carbon (EC and OC) on the daily samples on quartz-fiber filters were determined through thermal-optical transmission analysis with a Sunset EC/OC analyzer (Sunlab), using the NIOSH5040 protocol [52] [NIOSH, 1999] corrected for temperature offsets. NIOSH5040 protocol lasts about 12 minutes and the highest reached temperature is 940 °C. The instrument was calibrated with a TOC Standard Solution before starting the analysis.

2.4. Oxidative and reducing potential

One sampling line operated with PTFE filters was devoted to oxidative and reducing potential assessment; each filter was extracted in 10 mL of deionized water by rotating agitation at 60 rpm for 30 minutes. The obtained solution was then filtered through a nitrocellulose filter and split into proper aliquots for the dithiothreitol (DTT), ascorbic acid (AA) and 2′,7′-dichlorofluorescein (DCFH) OP assays (OP^{DTT}, OP^{AA}, OP^{DCFH}), and for the 2,2-diphenyl-1-picrylhydrazyl (DPPH) reducing potential (RP) assay (RP^{DPPH}). The OP and RP analytical measurements followed the methods reported in [53, 54, 55] [Frezzini et al. (2019 and 2021) and Massimi et al. (2020b)].

A parallel sampling on quartz-fiber filters was devoted to water soluble and total OP determination by the dithiothreitol (DTT) assay. The adopted procedures are those by [56, 57] Cho et al. (2005) and Verma et al. (2009), for the water soluble OP, and by [58] Gao et al. (2017), for the total OP. For the water soluble OP determination filter portions were extracted in deionized water by gentle shaking (30 min) and the extracts were filtered using a PTFE 0.45 μm pore syringe filters to remove insoluble materials and filter debris.

For the determination of the total aerosol OP, the procedure was similar to the one described above, with only one notable difference. The quartz fiber filter aliquots were not removed from the extraction solution after the end of the extraction procedure and they were kept in the primary vial while performing the DTT assay, in order to allow both soluble (in the extract) and insoluble (attached to the filter) aerosol components to react with the DTT. Total OP determinations are still ongoing and the results will not be discussed in the present work. More details about the experimental procedure are presented in the Supplementary Material.

At the urban background site high-time resolved (2-h time resolution) OP was measured through the 2′,7′-dichlorofluorescein (DCFH) assay (OP^{DCFH}) employing a particle-into-liquid sampler (PILS), which allows for continuous PM collection of a diluted solution of soluble species with suspended insoluble particles [59] [Simonetti et al., 2018a]. The sampling line was equipped with a PM_1 inlet and a denuder line to keep acid and basic gasses out of the sample. This technique does not guarantee the complete recovery of small and hydrophobic particles because particle growth is achieved through water condensation [60] [Costabile et al., 2019].

 doi:10.20944/preprints202204.0107.v1

2.5. Meteorological Measurements

To consider mean and turbulent atmospheric processes during the RHAPS field experiment, the meteorological variables (temperature, relative humidity, pressure, wind speed, solar radiation) were measured by a standard meteorological instruments (Lufft weather station WS700) with 1-min time resolution, while to measure the turbulence affecting the atmospheric processes near the surface, high-frequency measurements of the three wind components u, v, w, and virtual temperature T_v were made with an ultrasonic thermometer-anemometer uSonic-3 by Metek (sampling frequency 10 Hz) installed at height z = 3.3 m a.g.l. From these measurements we computed the wind speed and direction as well as the fluctuations u′, v′, w′, and T_v' with respect to the 1-h linearly detrended mean wind components (<u>, <v>, <w>) and virtual temperature $<T_v>$ ($u' = u - <u>$, $v' = v - <v>$, $w' = w - <w>$, $T_v' = T_v - <T_v>$). We estimated the sensible heat flux $H_0 = \varrho c_p w' T_v'$ (ϱ is the air density, c_p is the specific heat capacity of air at constant pressure) and turbulent kinetic energy TKE = 1/2 ($u'^2 + v'^2 + w'^2$) and the stability parameter z/L , where L is the Obukhov length. H_0 provides a measure of the thermal mixing capability of the atmosphere. TKE represents the intensity of turbulence produced by fluid shear, friction or buoyancy, or through external forcing. As both H_0 and TKE vary significantly in time and in space, they need to be monitored continuously.

2.6 Toxicological Data

2.6.1. Filter-based toxicological assays

To characterize the toxicological effects of PM_1 water-extracted from PTFE filters, different in vitro models representative of human lung tissue and targeted cells were used (e.g. BEAS-2B, THP-1). In order to assure the comparability with OP measurements, the extraction procedure (see Supplementary Material) was exactly the same and was carried out in the same days as toxicological measurements. Cells were exposed to increased dilutions of extracts for different times (30 min, 1, 3 and 24 h). After exposure, as indicator of unwanted biological effects cell viability (e.g. MTT reduction assay, PI staining, oxidative stress), release of inflammatory mediators (e.g. IL-8), genotoxicity and mutagenicity (e.g. alkaline comet assay, micronucleus test) were investigated [11, 61] [Corsini et al., 2013; Corsini et al., 2017a]. In parallel, to evaluate embryotoxicity, the effects of extracts were tested in Xenopus laevis embryos. Xenopus laevis embryos were exposed during the whole R-FETAX test period (from midblastula to tadpole, according to [62] [Battistoni et al., 2022) to the soluble extracted fraction diluted 1:10 in maintaining solution (see details in Supplementary Material). At the end of the test, tadpoles were morphologically observed under a dissecting microscope (Leica). The developmental degree (to evaluate old- and young-for age embryos) was evaluated according to [63] [Brown and Fabro (1981)] developmental scoring system adapted to Xenopus laevis considering the normal table of X. laevis development [64](Nieuwkoop et al., 2020) (details in Supplementary Material). Tadpole length was measured in order to evaluate small- and large-for age embryos. Statistical analysis was performed comparing data to controls.

2.6.2. ALI

In parallel with PM sampling and subsequent laboratory extraction and exposure, during the SIOPs (Table 1), environmental exposure of air liquid interface cultured cells BEAS-2B according to [15] [Gualtieri et al (2018) were used. Expression of oxidative, inflammatory and DNA damage related genes were quantified together with measurements of IL-8 and genotoxicity/mutagenicity (e.g. alkaline comet assay, micronucleus test).

2.7. Laboratory Measurements

The laboratory experiments were conducted in an atmospheric simulation chamber (ASC) and specifically at ChAMBRe (Chamber for Aerosol Modelling and Bio-aerosol

 doi:10.20944/preprints202204.0107.v1

Research) [65, 66, 67] [Massabò et al., 2018; Danelli et al., 2021; Vernocchi et al., 2021] in Genoa (www.labfisa.ge.infn.it), which represents a unique facility in Italy. ChAMBRe is a stainless-steel chamber, with a volume of about 2.2 m^3; scattered all over the main body, there are ISO-K flanges, with different diameter, which permit the access to the inner volume. Connected to ChAMBRe, several instruments and online monitors (listed in the Supplementary Material) complete the facility. The whole set-up is managed by a custom NI Labview SCADA (Supervisory Control And Data Acquisition). Inside ChAMBRe, atmospheric conditions (i.e., both chemical and physical parameters) can be maintained and monitored in real time for periods long enough to reproduce realistic environments and to study interactions among their constituents.

During RHAPS, experiments were carried out starting from the exhaust of a soot generator (Mini Inverted Soot Generator - Argonaut Scientific Corp.). Well-characterized particles of BC [67] [Vernocchi et al., 2021], and different mixtures of them with other pollutants, were aged inside ChAMBRe by different mechanisms, such as exposition to oxidant agents (i.e., NO_2 and O_3). Additional seeds (i.e., $(NH_4)_2SO_4$ or NH_4NO_3) were used too. The relative humidity was adjusted at varying levels between experiments. In addition to the online monitors, filter samples were collected for offline analysis of oxidative potential and for in vitro toxicological screening.

2.8. Forecast System

In order to support campaign planning, a forecast modeling system was devised in the frame of RHAPS. Due to logistic constraints, the scheduling of each Super Intensive Observational Period (SIOP) had to be determined one week before its beginning. Thus, the modelling system was designed in order to provide medium-range forecast with one daily update. Due to limitations of the computational resources (a Linux server with 64 cores at 2.7 GHz and 128 Gb RAM), the modeling domains were designed at moderate horizontal resolution (12 km) in order to warrant a daily forecast extended to 16 days ahead.

The global meteorological initial and boundary conditions were taken from the Global Forecast System (GFS) freely provided by the National Centers for Environmental Prediction (NCEP) of the U.S. National Oceanic and Atmospheric Administration (NOAA). Each day, the operational forecast run at 06 UTC at 3-hourly and 1.0° x 1.0° resolution, up to 384 hours ahead, were automatically downloaded from the NOMADS archive (https://nomads.ncep.noaa.gov/).

The WRF meteorological model [68] (Skamarock et al., 2005) version 3.7.1 was used to dynamically downscale GFS forecast. We used two nested domains, covering respectively Europe at 36 km of horizontal resolution and Italy and 12 km, and having 33 vertical eta-levels up to 50 hPa, with 11 levels in the bottom 1 km and the first level about 25 m thick. The main model parameterizations adopted were those used in [69] (Falasca & Curci, 2018), with RRTMG radiation schemes, WSM6 cloud microphysics, Noah land surface model and Bougeault and Lecarrere boundary layer closure scheme.

The WRF meteorological simulation, was used to drive the chemistry-transport simulation using CHIMERE model [70] (Menut et al., 2013) version 2014b. We used two nested domains over Europe and Italy, respectively at horizontal resolution of 0.5° and 0.15°, with 12 vertical levels up to 500 hPa and the first level about 21 m thick. The emission inventories, boundary conditions, and model parameterization were the same used in [69] (Falasca & Curci, 2018), with anthropogenic emissions taken from the European Monitoring and Evaluation Programme (EMEP, http://www.emep.int) at 0.5° resolution over Europe and from the National Thematic Center for Atmosphere, Climate, Emissions (CTN-ACE) [71] (Deserti et al., 2008) at 5 km resolution over Italy. Biogenic emissions were calculated online using MEGAN model. The boundary conditions were taken from global models monthly climatology from LMDz-INCA for gases and GOCART for aerosol species. Chemistry was calculated with the MELCHIOR mechanism with

Preprints (www.preprints.org) | NOT PEER-REVIEWED | Posted: 12 April 2022 doi:10.20944/preprints202204.0107.v1

secondary organic aerosol scheme and we adopted an aerosol sectional model with 10 geometric size bins for particles with diameters from 40 nm to 40 μm.

3. Results and Discussion

Here we firstly present data and introduce the phenomenology observed during the RHAPS experiment. In the following sections, we give a synthesis with an outlook to companion papers where data are analyzed in more detail.

3.1. Meteorological Overview

3.1.1. Modeling system

In order to aid interpretation of measurements collected during the campaigns, we report here an overview of the meteorological situation at the synoptic scale during the two Intensive Observational Periods. To better describe the meteorology during the SIOPs, it is convenient to organize the present brief meteorological analysis in weekly time slots, showing the Tuesday-Friday average synoptic conditions.

3.1.1.1. Winter campaign

In Figure 2 we show the maps over Europe of the average geopotential height anomaly at 500 hPa with respect to the 1981-2010 mean from NCEP/NCAR Reanalysis during the winter campaign and in Figure 3 the time series of main meteorological variables recorded in Bologna.

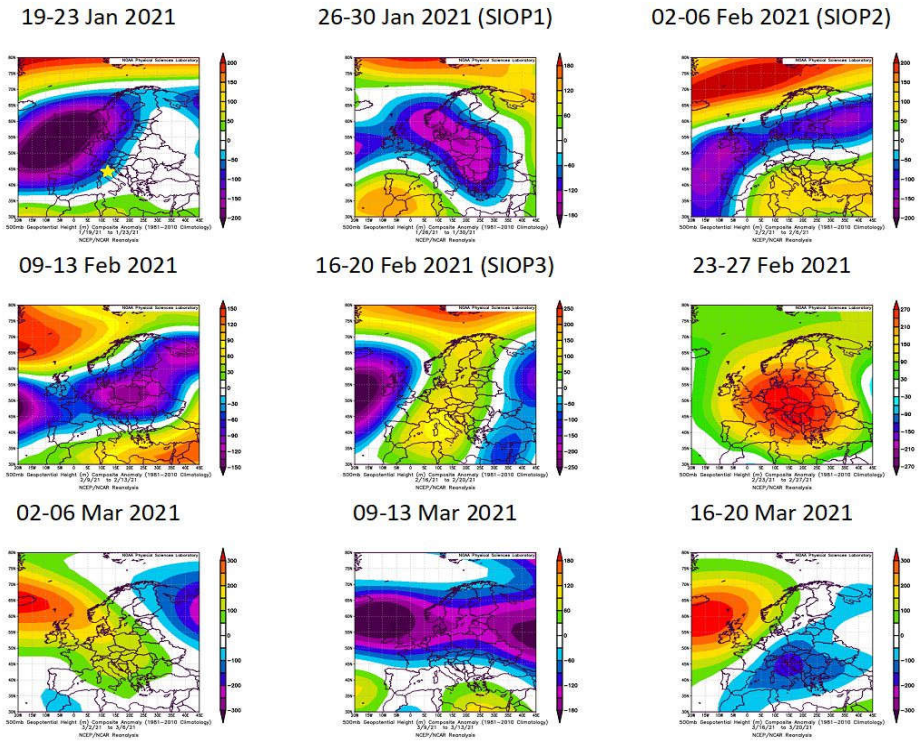

Figure 2. Average geopotential height anomaly at 500 hPa over Europe with respect to the 1981-2010 mean from NCEP/NCAR Reanalysis, during the Tuesday-Friday time slots of the winter Intensive Observational Period (IOP). The yellow star on the first map (top-left) denotes the location of the campaign. Cold colors (blue-purple) denote negative anomaly, warm colors (yellow-red) denote positive anomaly. Maps elaborated using the web tool of the NOAA Physical Sciences Laboratory (www.psl.noaa.gov).

Preprints (www.preprints.org) | NOT PEER-REVIEWED | Posted: 12 April 2022 doi:10.20944/preprints202204.0107.v1

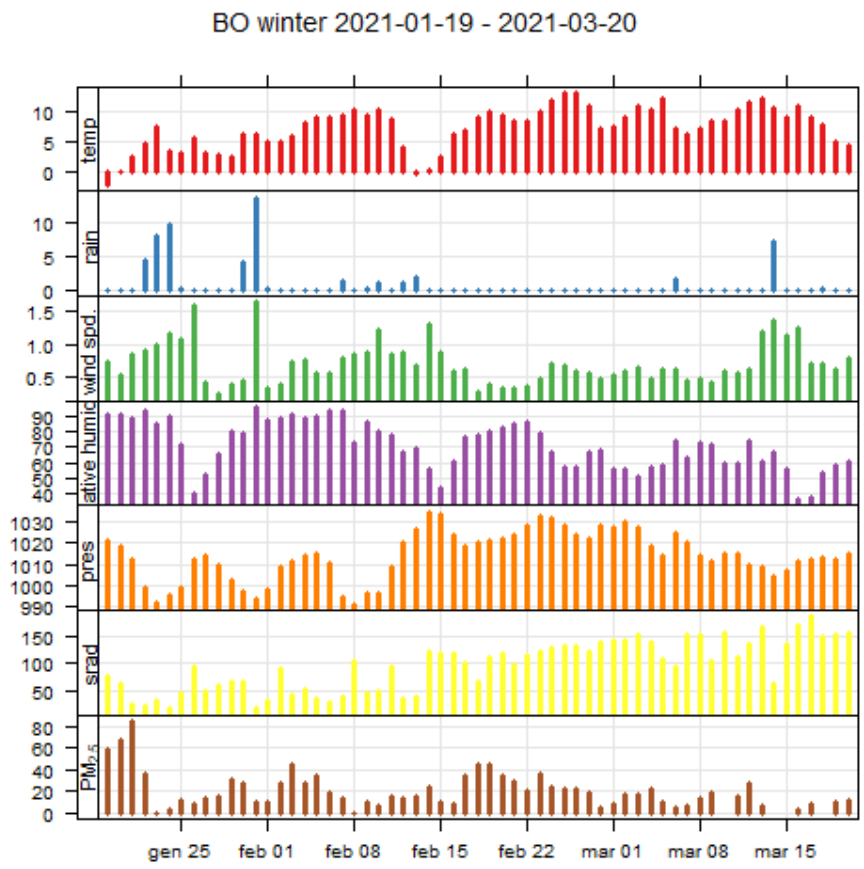

Figure 3. Hourly time series of meteorological variables recorded in Bologna during the winter campaign.

The first preparatory week (19-23 Jan) was characterized by a broad depression over Western Europe, which induced a south-westerly flow associated to cloudy and humid weather, with moderate wind speed, light rain and rising temperatures in Bologna area.

Starting from the second week (26-30 Jan), an anticyclonic ridge gradually mounted the Western Mediterranean basin, initially determining sunnier and drier conditions. The first SIOP took place in this week. As the anticyclone expanded eastward (02-06 Feb, SIOP2), the arrival warm southerly air masses over Western Europe favored the formation of low-clouds (and fog) with rising temperature and calm winds. A Saharan dust plume was also advected over the low-cloud deck by the end of the week (Figure S 1). The $PM_{2.5}$ mass concentrations were generally higher than the adjacent weeks during the two SIOP periods. In the following week (09-13 Feb), a cyclonic structure over Central Europe pushed the anticyclone to the South, driving a more zonal flow with moderate winds, some light rain, a sharp temperature drop, and a decrease in $PM_{2.5}$ mass concentration.

From the subsequent week (16-20 Feb, SIOP3), an anticyclone settled over Western-Central Europe, bringing sunnier weather with increasing temperatures and light winds from the East. These conditions favored the accumulation of pollutants near the surface, because of the reduced ventilation of the Po Valley, resulting in the highest $PM_{2.5}$ mass concentrations of the winter campaign (up to 50 μg m^{-3}). The prevailing anticyclonic circulation persisted in the last week of February and the first of March, but with slightly enhanced ventilation in the Po Valley, which resulted in generally lower $PM_{2.5}$ concentrations with respect to the SIOP3 period. An incursion of Saharan dust also took place in the area, with a peak on Feb 23 (Figure S 2). In the final period (09-20 Mar), low

Preprints (www.preprints.org) | NOT PEER-REVIEWED | Posted: 12 April 2022 doi:10.20944/preprints202204.0107.v1

pressure systems prevailed in Central Europe, yielding a few rain episodes, stronger winds and reduced $PM_{2.5}$ concentrations over the campaign location.

3.1.1.2. Summer campaign

In Figures 4 and 5 we show the maps of geopotential height anomaly and time series in Bologna for the summer campaign (Jun-Jul 2021). The first week (01-05 Jun) Western Mediterranean was under the influence of the southern offshoots of a high pressure system over Northern Europe, which determined a relatively cold air flow from the North, resulting in mild temperatures and light winds in the campaign area. The following week (08-12 Jun) the anticyclone was pushed eastward by a reinforcing low-pressure system over South-Eastern Europe, which brought clouds, rain and a modest reduction of $PM_{2.5}$ mass concentration.

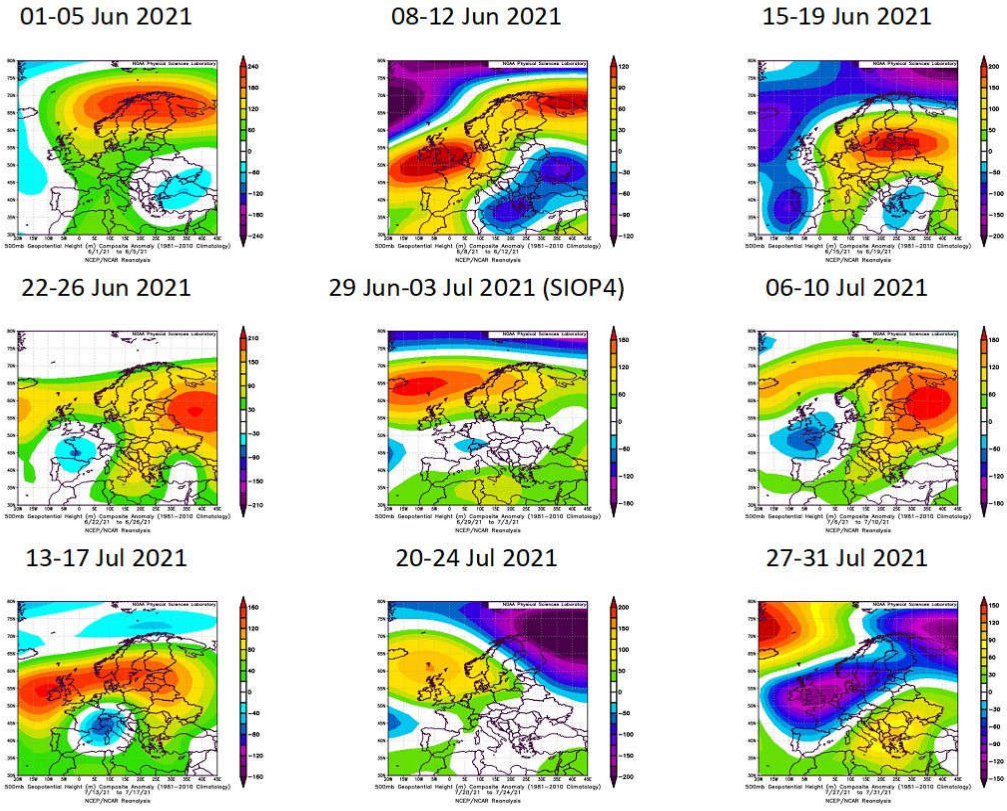

Figure 4. Same as Figure 2, but for the summer IOP.

Afterwards (15-26 Jun), a new anticyclone over Central Europe took the control of circulation over the Mediterranean basin, with south-easterly winds yielding high temperatures and dust advection from Norther Africa toward Italy. The peak of the dust event (20-21 Jun) was well visible from satellite imagery (Figure S3) and was reflected in the highest $PM_{2.5}$ concentrations during the campaign.

In the week that we selected for the SIOP4 (29 Jun-03 Jul) the pressure field over Southern Europe determined prevailing zonal winds, that prevented the arrival of new dusty air masses, but also favored enhanced ventilation of the Po Valley, with a consequent relative reduction of $PM_{2.5}$ concentrations. The synoptic scale pressure until middle July then settled again to a pattern determining prevailing flow from the South-East, with new dust advection Italy (not shown). The second half of July was characterized

Preprints (www.preprints.org) | NOT PEER-REVIEWED | Posted: 12 April 2022 doi:10.20944/preprints202204.0107.v1

by more variable weather, with more frequent cloudy sky, a few rain episodes, but yet with favorable conditions for the build-up of $PM_{2.5}$ concentrations

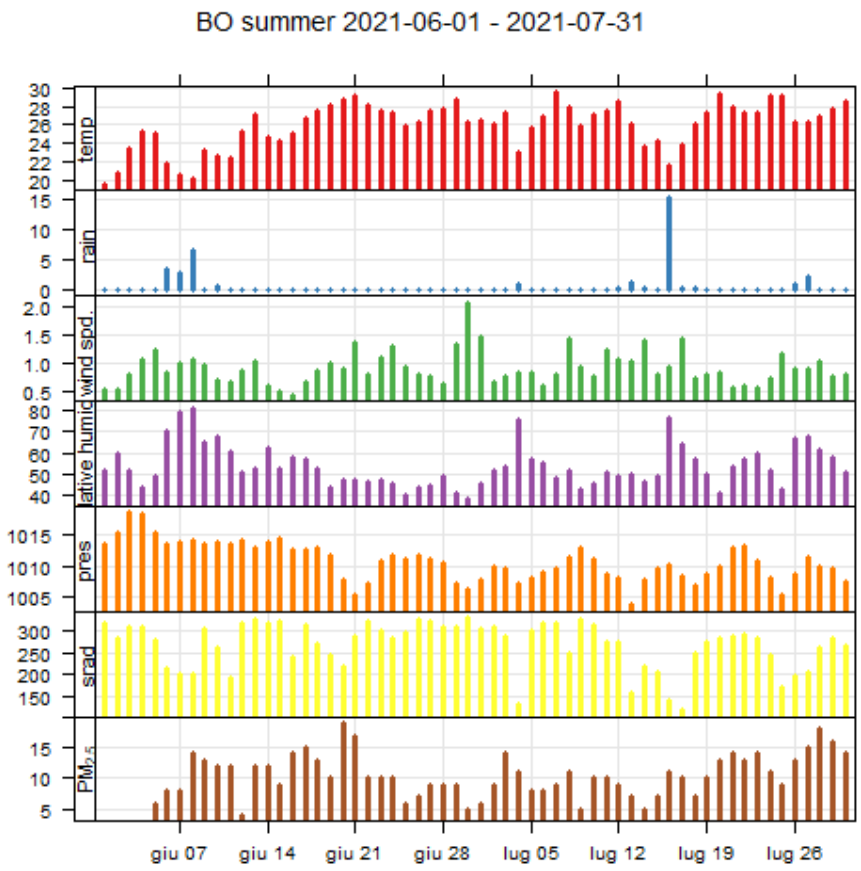

Figure 5. Same as Figure 3, but for summer campaign.

3.1.2. Assessment of the forecasting skills

The main motivation for the implementation of the operational forecast system was to provide information for the scheduling of the SIOPs, which had to be planned at least one week in advance. The main question was to support the field measurement strategy described in Sect.2.2 with the identification of source-specific aerosol types (Table 2) for which we aimed at selecting periods having favorable conditions for the accumulation of pollutants, the production of secondary aerosol, minimal interference from dust advected from the Sahara Desert. We thus looked for anticyclonic condition over the Western Mediterranean, low chance of advection from Sahara and low chance of rainy and windy conditions.

In Figure 6 we illustrate the broad forecasting skills of the modelling system. In panel (a) we display the decay of spatial correlation of the sea levels pressure field from GFS forecast as a function of daily lead time. We found a winter campaign-average correlation near 1 for the first three days and above 0.8 until day 7.

Preprints (www.preprints.org) | NOT PEER-REVIEWED | Posted: 12 April 2022 doi:10.20944/preprints202204.0107.v1

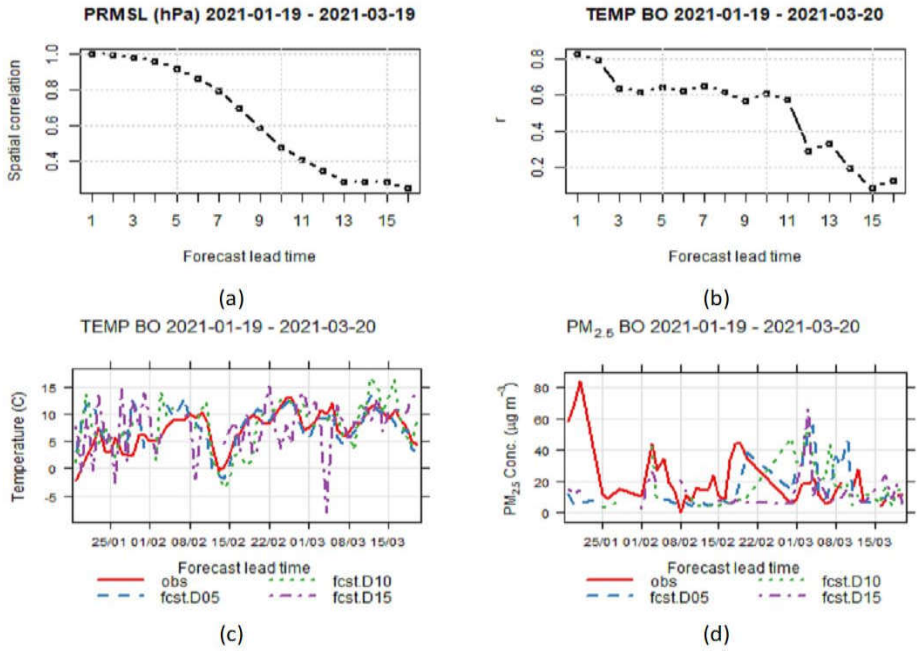

Figure 6. Illustration of forecast system skills during winter campaign. (a) Spatial correlation of sea levels pressure at 00 UTC from NOAA/GFS simulation between analysis and forecast days from 1 to 16. (b) Temporal correlation of daily mean temperature in Bologna from WRF simulation between analysis and forecast days from 1 to 16. (c) Timeseries of daily mean temperature in Bologna during winter campaign from observations and WRF simulation on forecast days 5, 10, and 15. (d) Timeseries of daily mean PM2.5 concentration in Bologna during winter campaign from observations and CHIMERE simulation on forecast days 5, 10, 15.

Afterwards, we found a sharper and gradual decrease down to 0.35 until day 13, and then a plateau until day 16. To understand the impact of the spatial correlation decay, we display in Figure 7 an example of the sea level pressure field averaged during a potential SIOP campaign week (from Tuesday to Saturday) obtained from the analysis (D00) and the forecasts 5, 10 and 15 days ahead, alternatively. The difference between the 5-day-ahead forecast the analysis looks very small: both the location and the magnitude of the main synoptic scale features are very similar, with only fine differences in the simulated patterns. At day-10 forecast time, more substantial differences emerge: the low pressure near Iceland is shallower with respect to the analysis, the high pressure over Northern Africa is less prominent, while high pressure over Eastern-Central Europe is more prominent, with the appearance of a secondary high pressure center over Scandinavia. At day-15 forecast time, the Iceland low is retreated northward by an expanded Azores high, and the high pressure over Central Europe is much less marked. However, over the Mediterranean basin general anticyclonic conditions, with air masses slowly advected from the southern quadrants, are deducible at all lead times. This relative stability and reliability at least of the very broad synoptic features over the area of interest (Northern Italy) was a common feature during the campaigns (both in winter and summer, see Figure S 4 for the latter), which made the information derived from the forecast system effectively useful for the SIOP scheduling.

Preprints (www.preprints.org) | NOT PEER-REVIEWED | Posted: 12 April 2022 doi:10.20944/preprints202204.0107.v1

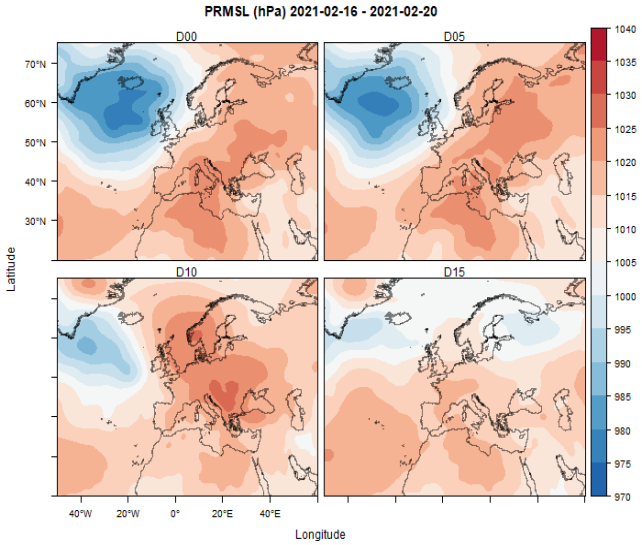

Figure 7. Average sea level pressure at 00 UTC from NOAA/GFS simulation in the period 16-20 Feb 2021 (SIOP3): maps for analysis (D00) and forecast 5, 10 and 15 days ahead (D05, D10, D15).

In panels (b-d) of Figure 6 we illustrate model skills from the local perspective. In panel (b) we show the temporal correlation as a function of lead time of the temperature in Bologna between the analysis (day-0) and the forecasts, averaged over the winter campaign period (for summer campaign refer to Figure S 4). We found a correlation of 0.8 until day-2, then a constant correlation around 0.6 until day-11, and a sharp decrease afterwards. For the summer case (Figure S 4 (b)), the correlation decay was more gradual. In panel (c) we compare the observed daily mean temperature timeseries in Bologna, with the timeseries from WRF forecasts at 5, 10, and 15 days lead time. The broad trend is captured at all forecast lead times, in terms of increasing and decreasing periods, but with increasing "noise" with increasing lead time. Remarkably, the drop of temperatures between 10 and 14 of February, and the subsequent reprise, was correctly anticipated at day-5 and day-10, but was less clear at day-15. This confirmed the reliability of forecast information at least of the broad features until at least day-10, which was enough for a correct scheduling of the SIOPs. In panel (d), we compare the observed $PM_{2.5}$ timeseries in Bologna with the timeseries forecasted with CHIMERE. The skill of the model here is more difficult to assess, given the generally larger bias with respect to the meteorological variables. For example, the enhanced concentrations in some subperiods (e.g. 02-06 Jan, 16-26 Feb, 02-05 Mar) were reasonably anticipated at day-5, but with much less reliability at day-10 and day-15. Indeed, the SIOP planning relied more heavily on an evaluation of the synoptic scale meteorological forecasts, rather than a point-wise evaluation of the chemical variables.

3.1.3. Micrometeorology

The time behavior of the temperature(a), wind speed (b),TKE (c), friction velocity (d), H_0 (e), and z/L (f) during the four Super Intensive Observational Periods. Winter SIOP1, SIOP2, SIOP3 and the summer SIOPS are shown in the Figures 1-4 from 0800 CET of one day to 0800 CET of the following day.

During SIOP1 (Figure 8) all the variables evidence a similar behavior with a peak around 1300-1400 CET with the exception of 30 January which presents between 0000-

Preprints (www.preprints.org) | NOT PEER-REVIEWED | Posted: 12 April 2022 doi:10.20944/preprints202204.0107.v1

0800 CET higher values of the temperature and the wind speed, and of all the variable related to mechanical mixing (u* and TKE). The larger values of the wind speed, sensible heat flux and of the variables related to the mechanical mixing are observed on 26 January. On this day, when sensible heat flux is negative, we observe values of TKE and U* larger than those of the other days of SIOP1. The mechanical mixing having peaks also during the afternoon until 0000 CET due to increasing values of the wind speed.

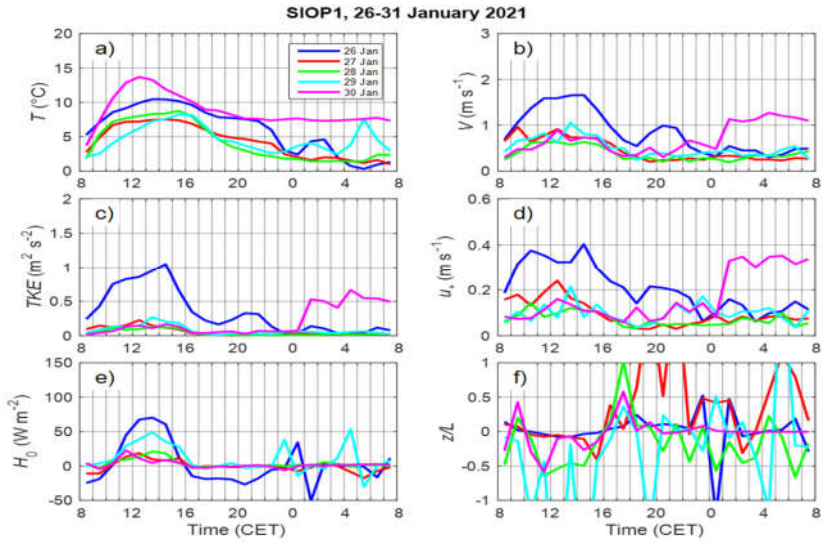

Figure 8. Temperature(a), wind speed (b), TKE (c), friction velocity (d), H_0 (e) and Z/L (f) during the winter SIOP1 from 0800 CET of one day to the 0800 CET of the following day.

SIOP2 (Figure 9) is characterized by low values of the wind speed, TKE, u* and temperature without a significant diurnal variation, this behaviour is typical of cold and foggy days. The values of the sensible heat flux are below 50 W/m^2 with the exception of day 2 February that evidences a weak diurnal behavior with characteristics similar to those of SIOP1.

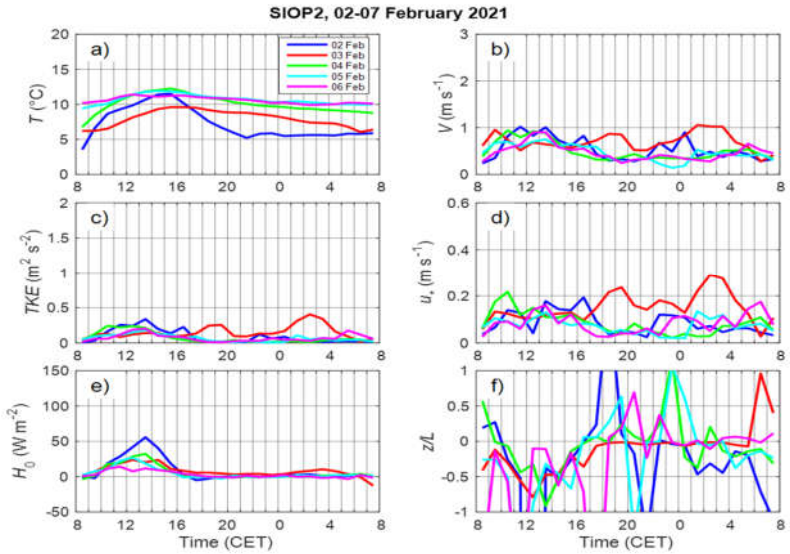

Figure 9. Temperature(a), wind speed (b), TKE (c), friction velocity (d), H_0 (e) and Z/L (f) during the winter SIOP2 from 0800 CET of one day to the 0800 CET of the following day.

Preprints (www.preprints.org) | NOT PEER-REVIEWED | Posted: 12 April 2022 doi:10.20944/preprints202204.0107.v1

During SIOP3 (Figure 10) all the variables show a similar behavior with weak convection between 0800-1600 CET and peaking (all but temperature) between 1200-1400 CET. During SIOP4 (Figure 11), the registered values are those typical of summertime.

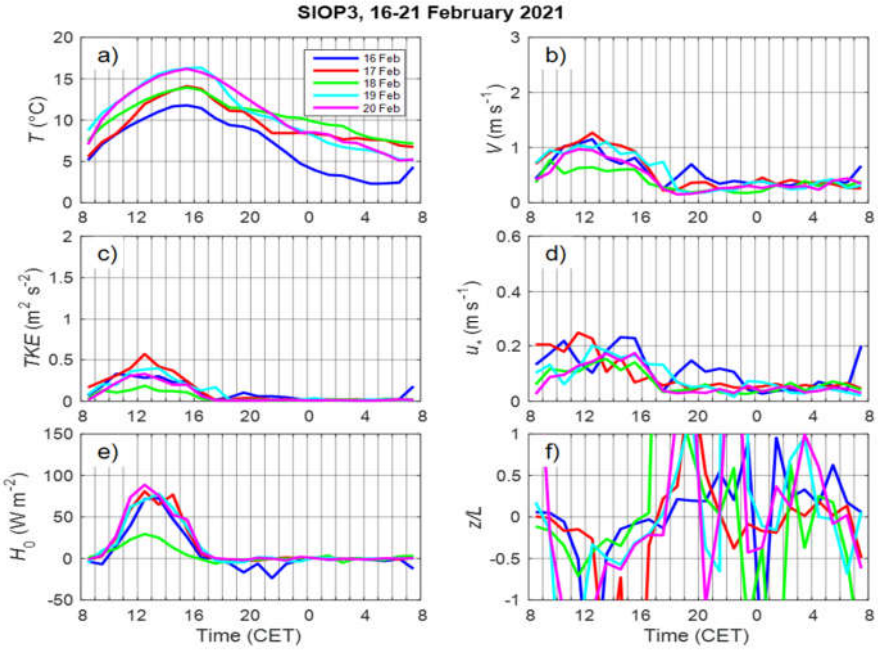

Figure 10. Temperature(a), wind speed (b), TKE (c), friction velocity (d), H_0 (e) and Z/L (f) during the winter SIOP3 from 0800 CET of one day to the 0800 CET of the following day.

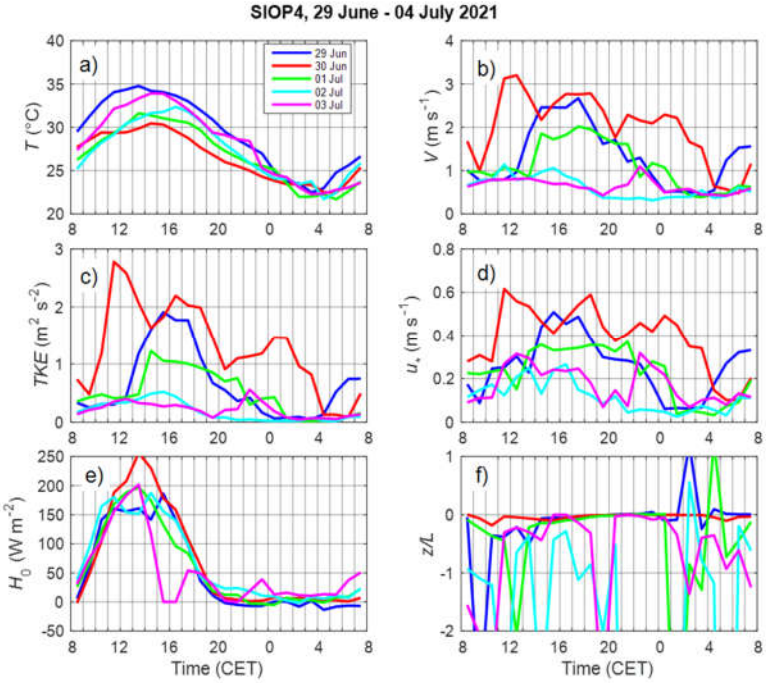

Figure 11. Temperature(a), wind speed (b), TKE (c), friction velocity (d), H_0 (e) and Z/L (f) during the winter SIOPS from 0800 CET of one day to the 0800 CET of the following day.

Maximum daily temperatures are between 30° and 35 °C; minimum temperatures are around 22°C in the early morning. The diurnal behavior of temperature and H_0 was

Preprints (www.preprints.org) | NOT PEER-REVIEWED | Posted: 12 April 2022 doi:10.20944/preprints202204.0107.v1

regular during all days. However, the wind regime in this period was variable and not regular. The first three days, 29 and 30 June, and 1 July were characterized by moderate (for this site) wind speed between 2 and 3 m s^{-1}. On the next days, 2 and 3 July, very weak wind < 1 m s^{-1} occurred. The most windy day was 30 June. The values of u* and TKE followed the behavior of wind intensity. The values of the stability parameter z/L indicate the predominance of convective conditions between 0800 and 1600 CET. The occasional presence of unstable stratification also in evening and nocturnal hours is probably due the strong heating of the underlying surface covered with asphalt which conserves higher temperature during late hours.

3.2. Aerosol Characterisation

3.2.1. PM_1 assessment during IOPs

Results from daily samples are shown in Figures 12-15 where median (box plot), interquartile range (box plot), 9-95th percentiles (whisker plot) of PM_1 chemical components and PM_1 mass concentrations are reported. Concentration values (in μg m^{-3}) detected at the urban background site of BO during the winter and summer campaign as well as at the rural site of SPC (only during winter) are shown. PAHs concentrations were measured at both sites during winter only and they are reported in pg m^{-3}.

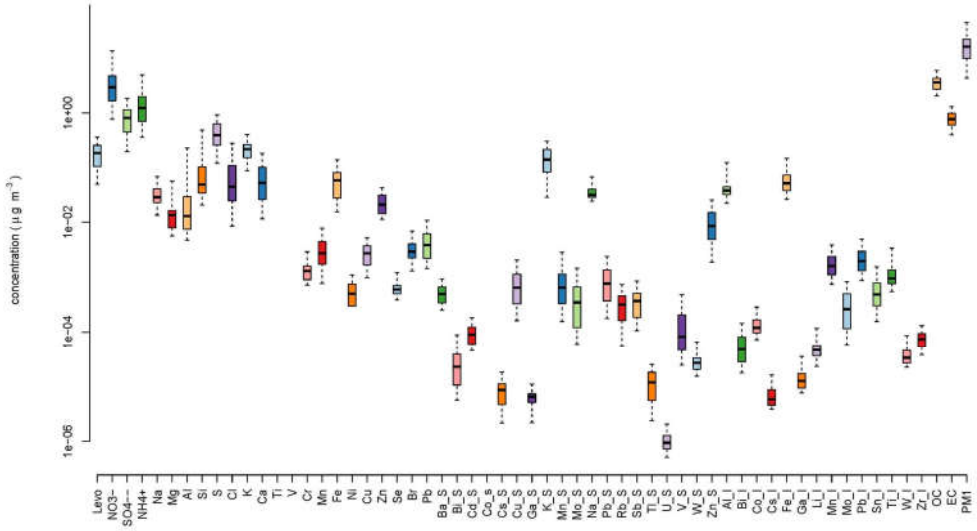

Figure 12: Overview of median (box plot), interquartile range (box plot), 9-95th percentiles (whisker plot) of PM_1 chemical components detected at the urban background site of BO during the winter campaign.

Preprints (www.preprints.org) | NOT PEER-REVIEWED | Posted: 12 April 2022 doi:10.20944/preprints202204.0107.v1

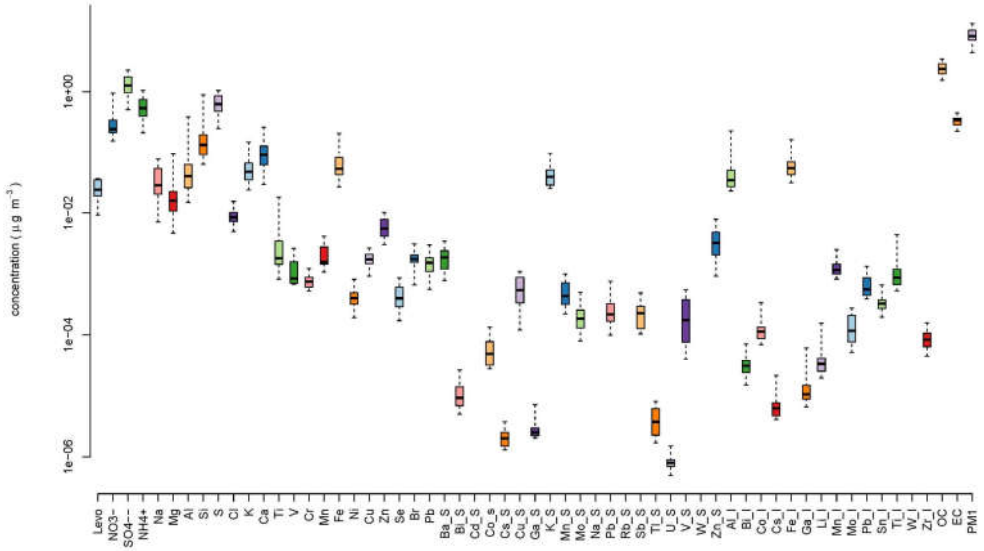

Figure 13. Overview of median (box plot), interquartile range (box plot), 9-95th percentiles (whisker plot) of PM_1 chemical components detected at the urban background site of BO during the summer campaign.

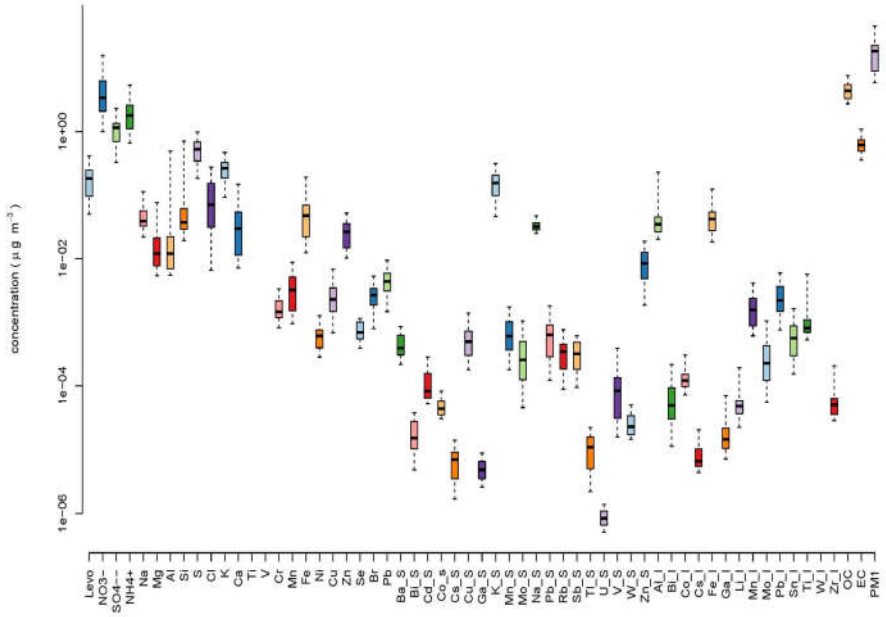

Figure 14. Overview of median (box plot), interquartile range (box plot), 9-95th percentiles (whisker plot) of PM_1 chemical components detected at the rural site of SPC during the winter campaign.

Preprints (www.preprints.org) | NOT PEER-REVIEWED | Posted: 12 April 2022 doi:10.20944/preprints202204.0107.v1

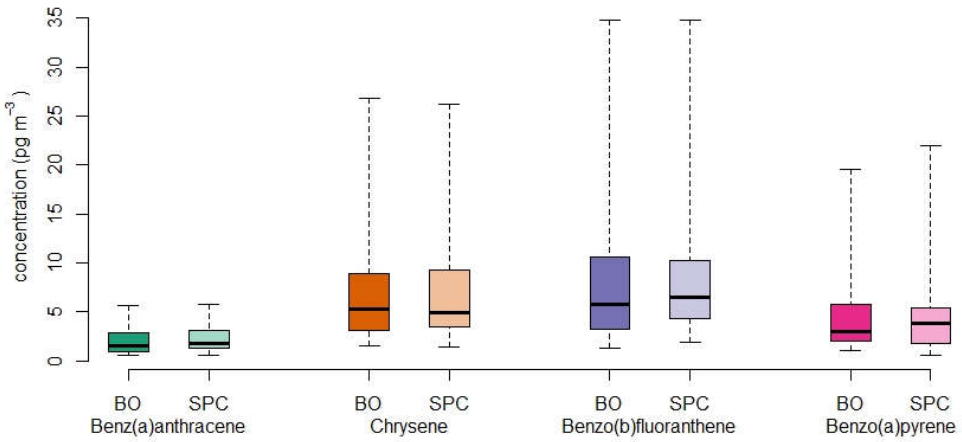

Figure 15. Overview of median (box plot), interquartile range (box plot), 9-95th percentiles (whisker plot) of PAHS detected in PM_1 samples at both sites during the winter campaign.

It is worth mentioning that the sampling period – especially during the winter campaign - was characterized by a reduced anthropogenic activity due to COVID-19 pandemic restrictions. During wintertime, there were no relevant differences (i.e., in general less than 20 - 25%) in average concentration values when comparing parallel samples collected at BO and SPC. PM_1 mass concentration was 18 ± 1 μg m^{-3} at both sites and it was mainly accounted for by secondary inorganic ions (i.e., sulfate, nitrate, and ammonium) together with organic carbon. As expected, due to the stronger atmospheric dilution conditions, summertime PM_1 concentrations were approximately a factor 2 lower than wintertime ones and the major components were sulfates and OC. As concerns PAHs concentrations at the urban background site, the most abundant species were benzo(b)fluoranthene and chrysene with average concentrations of 12 pg m^{-3} followed by benzo(a)pyrene (7 pg m^{-3}) and benz(α)anthracene (3 pg m^{-3}); at the rural site concentration values were slightly lower with 10 and 9 pg m^{-3} for benzo(b)fluoranthene and chrysene, respectively, and 6 pg m^{-3} for benzo(a)pyrene and 2 pg m^{-3} for benz(α)anthracene.

3.2.2. PM1 assessment during IOPs

Figure 16 shows the ranges of variability of PM_1 major components as measured at the urban site by the online equipment. Related statistics and data coverage are shown in Figure 17. We show first the mass concentration of PM_1, as reconstructed by SMPS data and validated on filter-based mass, after the procedure described in [14] Costabile et al. (2017). Then, PM_1 components, i.e. organic aerosol, nitrate, ammonium, sulfate, and BC mass concentration are reported. The total number concentration is then represented, together with total surface area concentration and relevant aerosol size representative of the entire aerosol population (calculated as median mobility diameter of the particle surface size distribution [72] (Costabile et al., 2017b). Finally, we show the alveolar Lung Deposited Surface Area corresponding to the particle surface area size distribution weighted with the associated lung deposition curve and integrated over the whole particle size, the inhalation fraction according to the ICRP model [43] (Hinds, 1999).

Preprints (www.preprints.org) | NOT PEER-REVIEWED | Posted: 12 April 2022 doi:10.20944/preprints202204.0107.v1

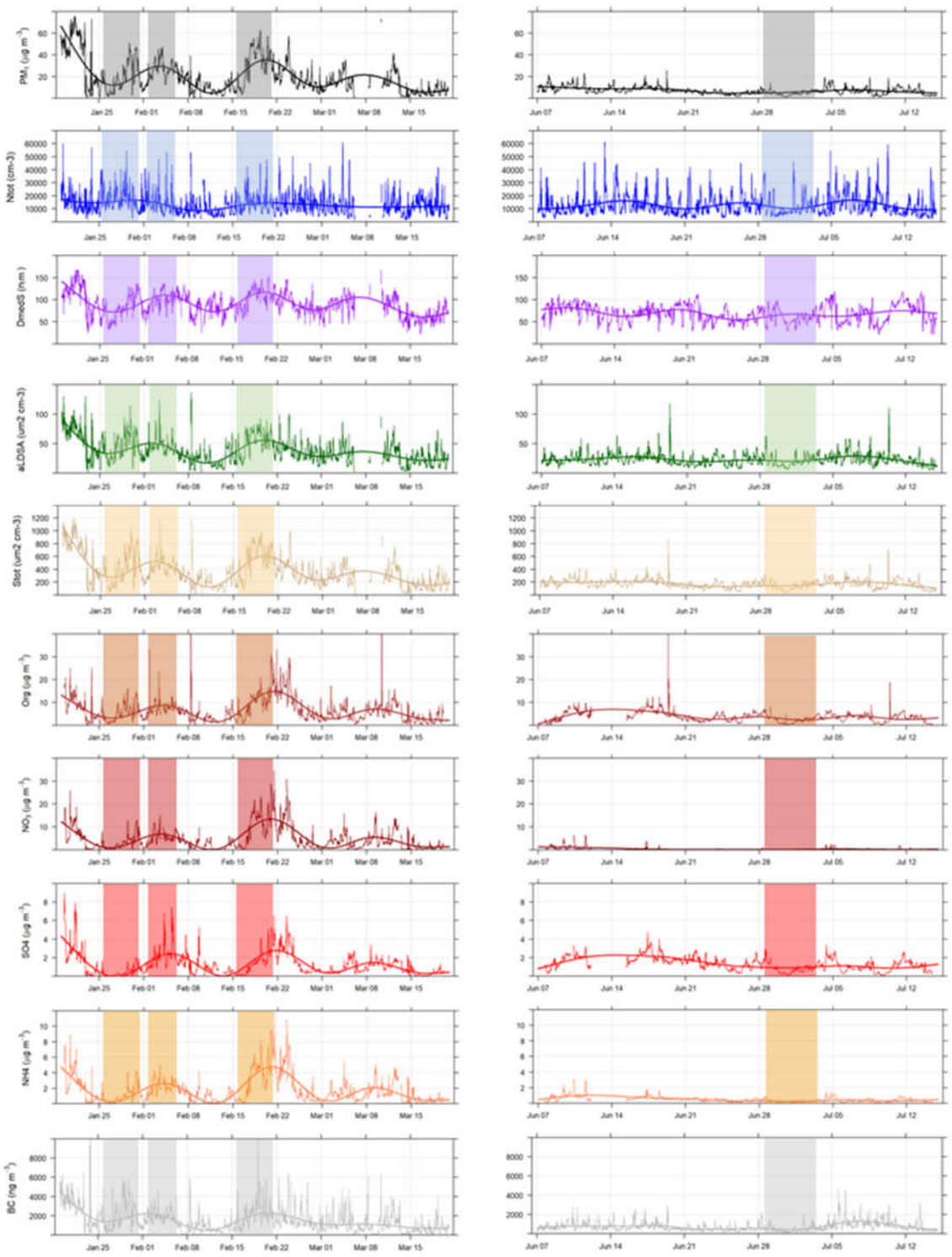

Figure 16. Time plot of selected aerosol properties during the winter and summer field campaigns. On the left, from top to bottom: mass concentration of PM1 (reconstructed by SMPS data), total number concentration (Ntot), surface-area median particle diameter (Dmed), alveolar Lung Deposited Surface Area (aLDSA) and total surface area concentration (Stot), Organic aerosol, nitrate, ammonium and sulfate, and BC mass concentration .

Preprints (www.preprints.org) | NOT PEER-REVIEWED | Posted: 12 April 2022 doi:10.20944/preprints202204.0107.v1

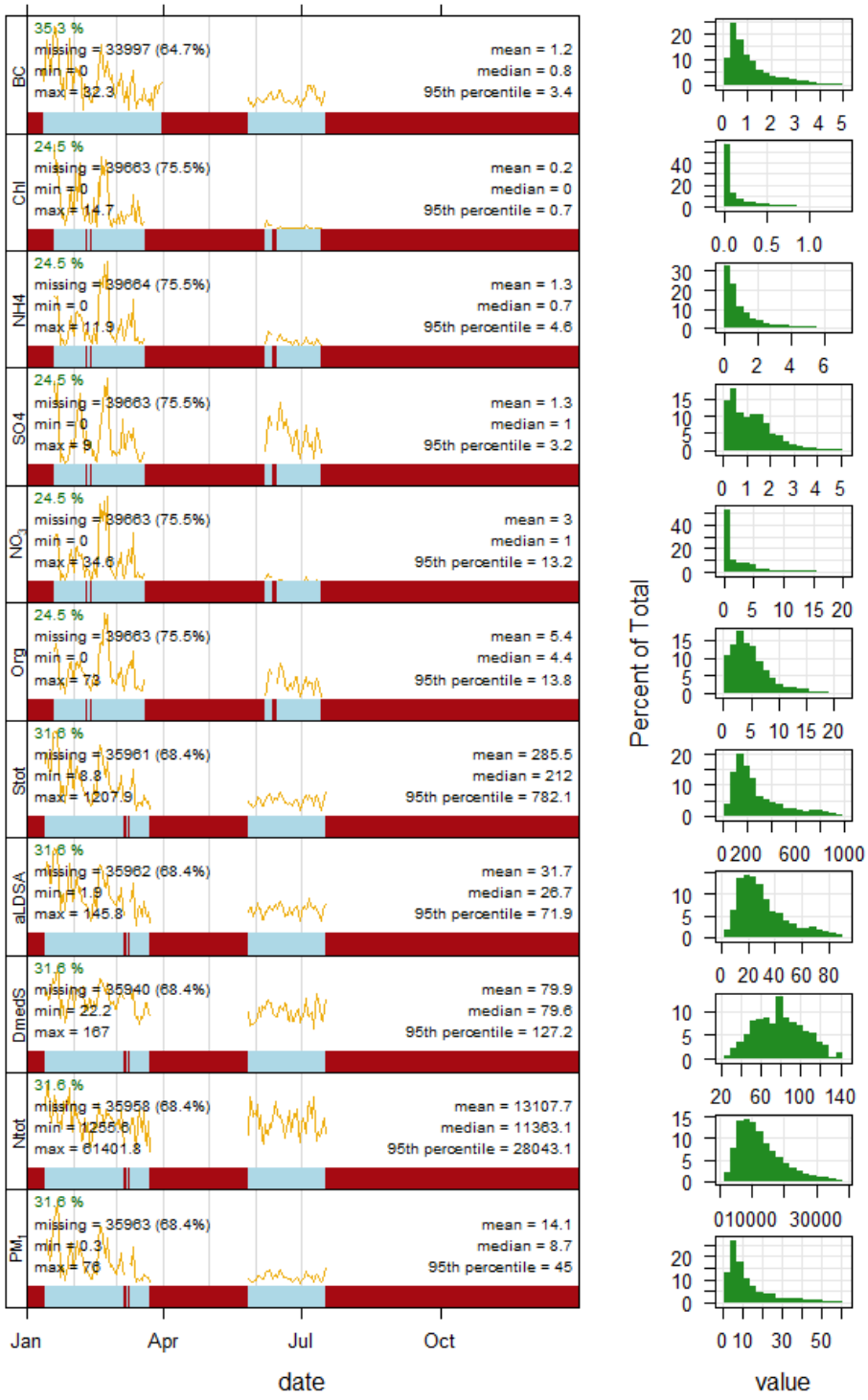

Figure 17. same as Figure 16, but including statistics and data coverages.

Statistical data of selected aerosol metrics are summarized in Table 4.

Table 4. Descriptive Statistics of selected aerosol metrics: PM1 (reconstructed from SMPS) and BC mass concentration, particle number (N_{tot}), alveolar Lung deposited surface area (aLDSA), and particle median diameter (D_{medS}).

Preprints (www.preprints.org) | NOT PEER-REVIEWED | Posted: 12 April 2022 doi:10.20944/preprints202204.0107.v1

		Winter (11/01/21 - 31/03/21)				Summer (27/05/21 - 17/07/21)			
	UoM	**Mean**	**Std.Dev.**	**Median**	**Range (min-max)**	Mean	Std. Dev.	Median	Range (min-max)
PM1	µg/m³	20.04	15.40	15.60	0.28 - 75.96	6.61	3.26	6.12	0.93 - 25.64
N_{tot}	cm³	13337.83	7440.54	11928.46	1255.62 - 61401.84	12817.42	7775.75	10586.14	2018.21 - 61312.12
D_{medS}	nm	90.51	26.11	92.04	22.21 - 167	66.59	19.38	66.20	22.21 - 119.05
a-LDSA	µm²/cm³	38.99	21.70	35.22	1.87 - 145.76	22.59	9.45	21.24	4.59 - 117.37
BC	ng/m³	1495.88	1241.26	1163.00	6 - 32275.11	677.32	456.41	551.16	33 - 8463.1

As a general feature, we note that particle mass (and surface) concentrations and diameters were on average larger in winter than in summer, whereas total particle number concentration and only sulfate mass concentration show conversely on average similar values in winter and summer time. The behavior of the particle number and relevant diameters is shown in more detail in Figure 18.

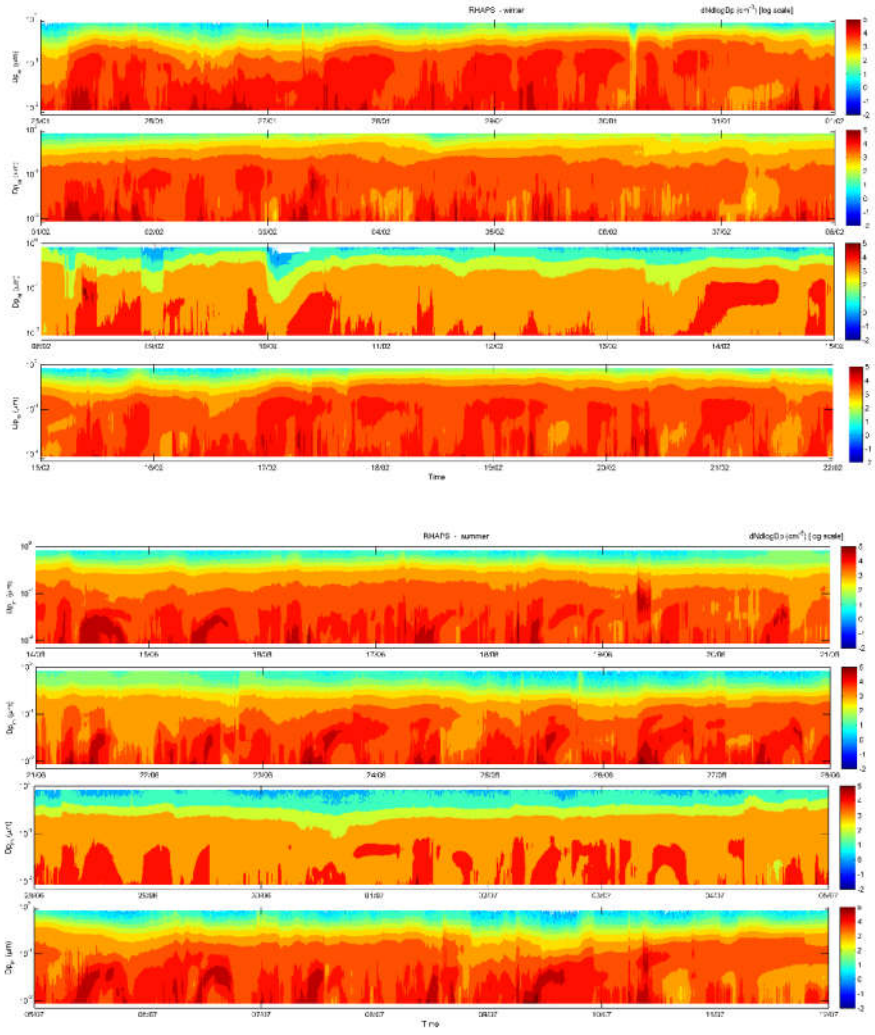

Figure 18. Full particle number size distribution measured in selected periods of the winter and summer IOPs, including the four SIOPs.

These differences reflect different processes, dynamics and sources governing the atmospheric aerosol in winter as compared to summer, and the ability of the related metrics (i.e., number, mass, size of particles) to capture these. For example, in wintertime, higher combustion-related emission sources coupled to lower atmospheric mixing can result in higher particle mass - at least for BC. This is not necessarily the case for the total

Preprints (www.preprints.org) | NOT PEER-REVIEWED | Posted: 12 April 2022 doi:10.20944/preprints202204.0107.v1

particle number, which is also significantly influenced by new particle formation (NPF) events. The smaller particle diameters in summer may likely be due to these different NPF rates in winter as compared to summer coupled to the higher accumulation in the atmosphere (and hence particle ageing) in winter. These topics will be analyzed in future publications. Here we note that these general features do reflect into the selected SIOPs. SIOP4 (30 Jun - 3 Jul 2021), covering a summer period, shows the lowest concentrations of all variables except the particle number. Note a NPF event occurring during SIOP4 (on 2 July), but no NPF occurring during the winter SIOPs. Both SIOP1 (26 - 30 Jan 2021) and SIOP3 (16 - 20 Feb 2021) cover winter conditions with increasing concentrations and particle diameters (accumulation in the atmosphere). SIOP3 shows higher mass concentrations than SIOP1, which in turn shows higher number concentrations with smaller particle size. SIOP2 (2 - 6 Feb 2021) covers a period of stable concentrations, with some foggy conditions.

3.3. Oxidative and Reducing Potential

Oxidative and reducing potentials of the 24-h PM_1 samples collected at BO and SPC during the winter and summer monitoring periods are summarized in Table 5.

Table 5. Oxidative and reducing potentials of the 24-h PM_1 samples collected at BO and SPC during the winter and summer monitoring periods.

			OP^{DCFH}	OP^{AA}	OP^{DTT}	OP^{DTT}_{QRTZ}	RP^{DPPH}
		UoM	nmol H_2O_2 m^{-3}	nmol AA min^{-1} m^{-3}	nmol DTT min^{-1} m^{-3}	nmol DTT min^{-1} m^{-3}	% Cons DPPH m^{-3}
		MDL	1.0E-10	0.01	0.006	0.08	0.008
BO	**Winter**	**Mean**	4.7E-09	0.37	0.91	0.58	0.42
		SD	*3.1E-09*	*0.35*	*0.55*	0.25	*0.42*
		Median	4.1E-09	0.27	0.83	0.53	0.33
		min-max	1.1E-10 - 1.2E-08	0.018 - 1.9	0.087 - 2.5	0.15-1.1	0.25 - 1.8
	Summer	**Mean**	1.6E-09	0.47	0.31	0.22	0.045
		SD	*1.4E-09*	*0.54*	*0.17*	0.10	*0.087*
		Median	1.5E-09	0.23	0.31	0.22	0.046
		min-max	7.3E-10 - 4.6E-09	0.022 - 2.5	0.016 - 0.66	0.09-0.57	0.15 - 0.23
SPC	**Winter**	**Mean**	6.3E-09	0.55	0.85	0.48	0.41
		SD	*3.9E-09*	*0.82*	*0.47*	0.23	*0.33*
		Median	5.8E-09	0.24	0.86	0.43	0.38
		min-max	1.9E-10 - 1.6E-08	0.010 - 4.6	0.006 - 2.0	0.22-1.2	0.11 - 1.3

From Table 5, we can observe that higher values of OP^{DCFH} and OP^{DTT} were measured at both sites in the colder period, characterized by less efficient mixing of air masses and greater accumulation of airborne pollutants. This shows that OP^{DCFH} and OP^{DTT}, as well as PM1 concentration, were mainly modulated by seasonal atmospheric stability. In fact, OP^{DCFH} and OP^{DTT} are known to be predominantly sensitive to finer particles [73, 74, 75] [Simonetti et al., 2018b; Manigrasso et al., 2020; Molina et al., 2020] that are more influenced by variations in atmospheric conditions and to domestic biomass heating [55, 76, 77] [Verma et al., 2018; Bates et al., 2019; Massimi et al., 2020b], which is more intense during winter. The same can be pointed out for RP^{DPPH}, indeed, the reducing capacity of PM_1 seems to increase in winter, as well as for OP^{DCFH} and OP^{DTT}. Although not much is

Preprints (www.preprints.org) | NOT PEER-REVIEWED | Posted: 12 April 2022 doi:10.20944/preprints202204.0107.v1

yet known about the PM reducing activity, these results highlighted the ability of RP^{DPPH} to predict PM_1 reducing properties. All of these assays seem to be less affected by inter-site variability. On the contrary, OP^{AA} appears to be less modulated by seasonal variations and more influenced by different contributions of the emission sources at the two sites. The daily contribution of the different emission sources to the oxidative and reducing capacity of PM_1 and the associated toxicological potential will be extensively evaluated in future studies.

3.4. Toxicological Assessment

3.4.1. Effects of PM_1 from water-extracted samples

Effects of PM_1 from water-extracted filter samples were investigated in BEAS-2B cells as surrogate of epithelial lung cells and THP-1 cells as surrogate of alveolar macrophages. For illustrative purposes, the results of IL-8 release in both cell types are reported in Figure 19.

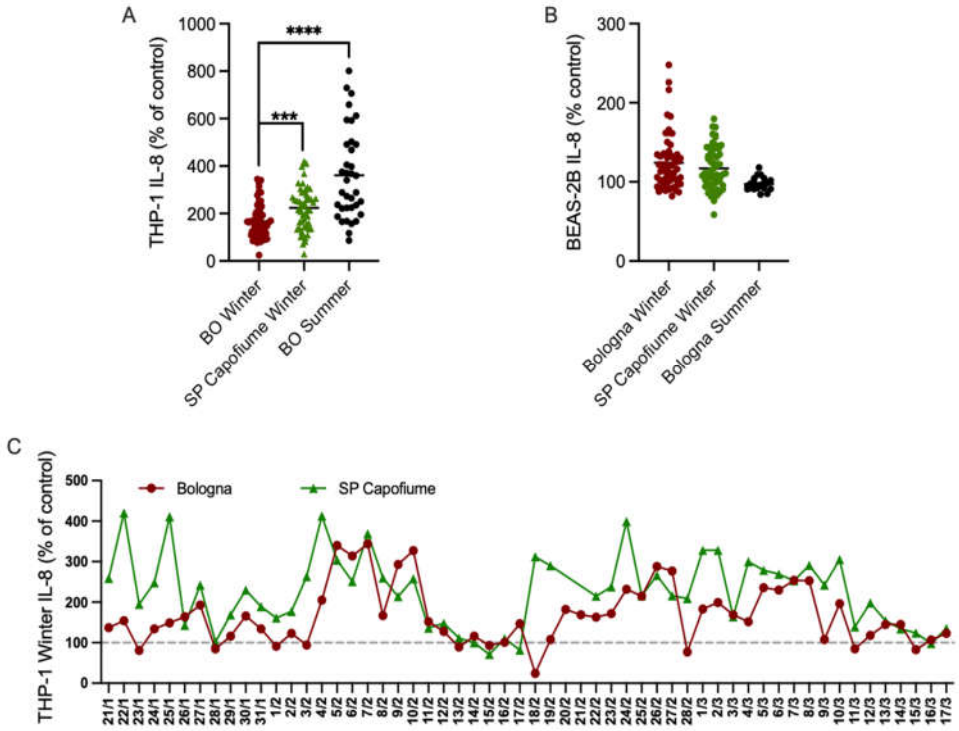

Figure 19. Seasonal and site effects of PM_1 water-extracted filters on IL-8 release. BEAS-2B and THP-1 cells were exposed to 1:10 dilution of the extracts for 24 h. A) Average responses in exposed THP-1 cells. B) Average responses in exposed BEAS-2B cells. C) Daily IL-8 release in THP-1 cells exposed to extracts obtained from winter samples. Asterisks indicate statistical significant differences among groups as evaluated by unpaired Student t test.

Results are expressed as % of control. In THP-1 cells, seasonal and site differences were observed in average responses, with higher releases observed in SPC compared to BO, and higher production in summer vs winter samples obtained in BO. In addition, daily differences in IL-8 release were also observed. Regarding the release of IL-8 in BEAS-2B cells, no seasonal or site differences in the average responses were found. In the majority of the samples the release of IL-8 was above control values. These results confirm the ability of the models used to respond to PM_1 water-extracted filters, with a different sensitivity between the two models and in relation to specific components.

3.4.2. Effects in air liquid exposed cells.

Preprints (www.preprints.org) | NOT PEER-REVIEWED | Posted: 12 April 2022 doi:10.20944/preprints202204.0107.v1

The average responses in exposed cells shows a non-significant difference between winter and summer campaigns except for a significant difference in Cxcl-8 gene expression (p = 0.04, ANOVA) and IL-8 release (p = 0.02, ANOVA) that were higher in winter samples (Figure 20). A slight but not significant increase in winter samples is reported also for NQO1 and HMOX genes. However, differences among the different days of exposure are evident as for the scatterplot properties and this distribution of the responses may indicate an altered gene expression in relation to specific aerosol properties.

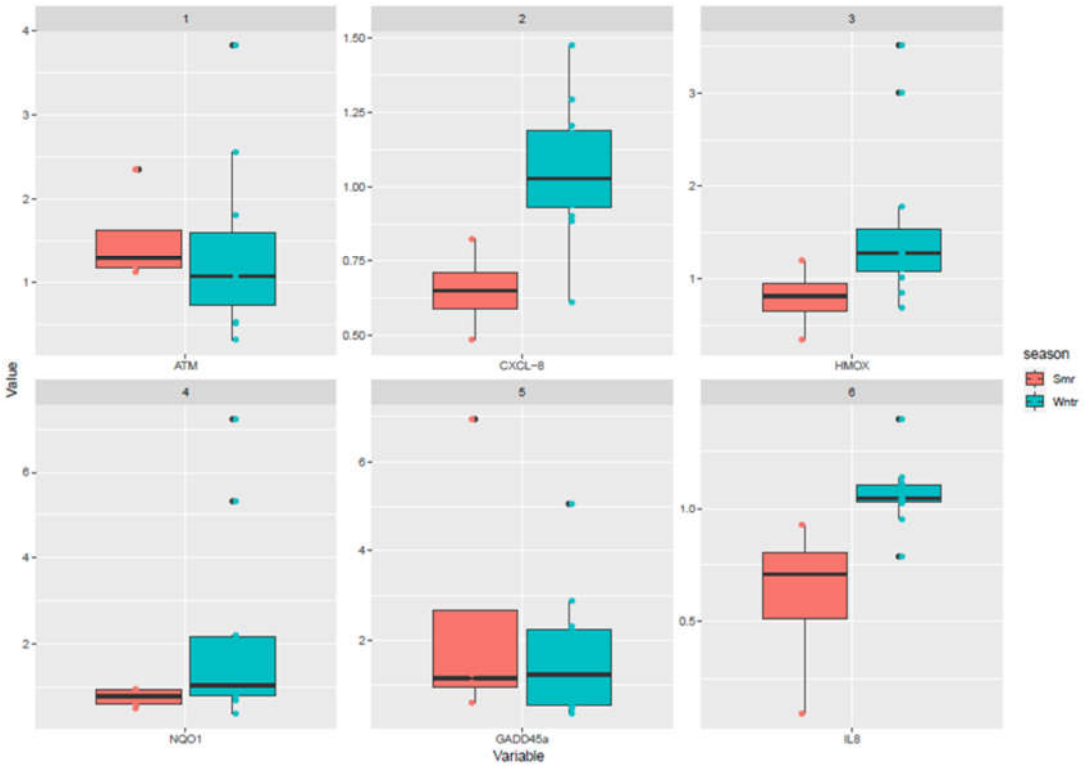

Figure 20. Overview of median (box plot), interquartile range (box plot), 9-95th percentiles (whisker plot) of genes characterized in ALI exposed lung cells. Significant differences were observed for Cxcl-8 gene (p =0.04, ANOVA) and for the subsequent release of the IL-8 protein (p = 0.02,ANOVA) with higher expression and release in winter compared to summer exposures.

3.4.2. Embryotoxicity

Embryo represents a complex biological model responding to environmental signals blocking, changing the speed of development or altering the normal morphogenetical pattern. Nor lethal or malformative effects were recorded after the exposure to the water extract fraction. By contrast, significant effects were observed as developmental degree variations (embryos old-/young-for age or large-/ small- for age) in extract from specific days (Figure 21).

Preprints (www.preprints.org) | NOT PEER-REVIEWED | Posted: 12 April 2022 doi:10.20944/preprints202204.0107.v1

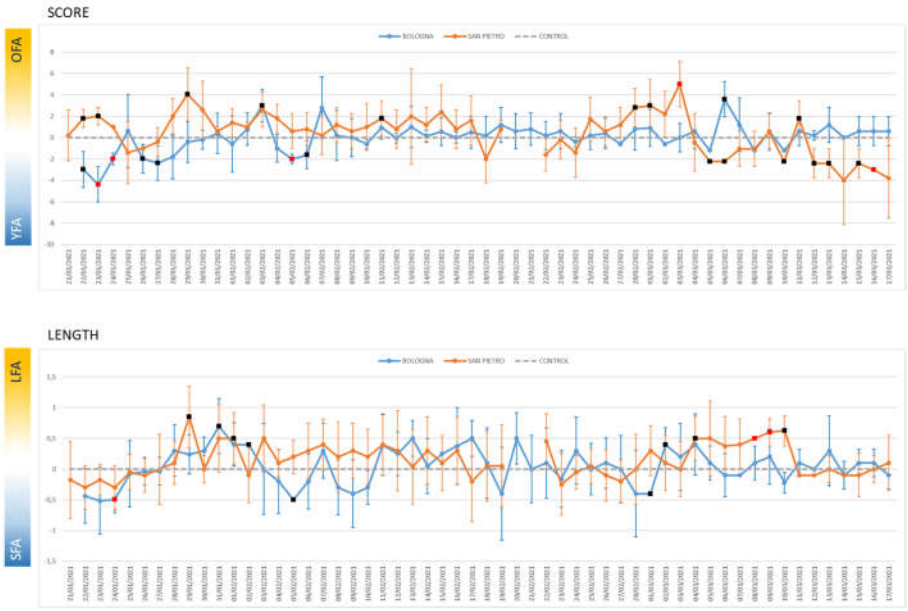

Figure 21. Development degree variations of the winter season reported as old-/young- for age (OFA/YFA) or large-/small- for age (LFA/SFA). Significance: black square $p<0.05$; red square $p<0.001$. Gray dotted line: control.

4. Conclusion and Outlooks

Linking air quality and health is still a complex issue. The debate on which particle type is more or less toxic [78] [Thurston et al., 2022] and how to protect human health [4, 79] [Stafoggia et al., 2022; Al-Kindi et al., 2020] is still unresolved, while the last WHO guidelines [1] (WHO 2021) tend to reduce as much as possible the thresholds of safety for human health, suggesting the absence of a safe threshold for $PM_{2.5}$. To target this topic, the RHAPS project was launched with the major objective to identify specific properties of PM_1 from combustion sources that are responsible for toxicological effects and can be used as new metrics for health-related outdoor pollution studies.

In this paper, we present the overall methodology of the RHAPS project, and introduce the phenomenology and the first data observed. These will be discussed in detail in a series of companion papers, the focus basically on four topics:

1. Source apportionment of PM_1 and the role of source emissions on aerosol toxicity
2. OP as a predictive variable for PM_1 toxicity with focus on SOA possessing redox-active capacity
3. Exposure-response relationships for PM_1
4. Air quality models to forecast PM1 toxicity.

The hypothesis to test is that the exposure to primary and secondary atmospheric aerosols under conditions representative of the real-life scenario in the atmosphere can differently activate oxidative stress and inflammatory responses. It is worth noting that the real life scenario is a major focus of the RHAPS project, where exposure is assessed to the real atmospheric concentrations, as pioneeringly proposed during the first CARE experiment [14] [Costabile et al., 2017]. Future papers (manuscripts in preparation) will investigate this by analysing physicochemical properties and specific metrics (both classical and newly developed) of source-specific primary and secondary aerosol, and exploring connections between all these metrics and the release of biological markers in lung epithelial cells, the focus on oxidative stress related pathways. Importantly, beyond PM_1 and BC mass concentration, we will include among these metrics the source-apportioned PM_1 oxidative potential, and statistical profiles of source specific aerosol types such as SOA. The assessment of the redox-active capacity of SOA will be derived by the comprehensive RHAPS assessment from in-field and laboratory measurements.

Anthropogenic aerosol secondary organic compounds, such as quinones, are considered among the most important players in determining OP [80] [Chung et al., 2006] and are known to generate from photochemical ageing of the emissions of a very broad range of combustion systems [9] [Jimenez et al.,2009]. The variability in aerosol properties and in OP will be specifically linked to changes in distinct source contributions with the novel source apportionment approach of RHAPS by inserting each data value in its original time schedule through advanced receptor modelling [81, 82, 83, 84] [Zhou et al., 2004; Ogulei et al., 2005; Forello 2019 e 2020]. The insertion of non-compositional variables (e.g. absorption coefficients or OP) in the same modeling process, the combination with fossil fuel and biomass burning EC and OC components from optical source apportionment as well as the organic aerosol components retrieved from the AMS apportionment will be key for a robust source identification and assessment. As the final step, the air quality modeling will be devoted to develop an operational air quality forecast tool of PM toxicity to be deployed on a national scale. Findings will be among the first results of this kind and have the potential to support the development of new metrics for health-related pollution studies, and contribute to the cutting-edge research on OP and SOA.

Supplementary Materials: The following supporting information can be downloaded at: www.mdpi.com/ Supplementary Material.

Author Contributions: "Conceptualization, F.Co., R.V., S.D., M.C.F.; methodology, F.Co., S.D., R.V., G.C., S.C., L.M., M.G., M.Ri., D.M., P.P., S.A., E.C., M.B., M.P., F.L., C.P.; modeling, G.C., R.V., F.C., A.C.F.; validation, M.Ri., F.Co., M.P., L.M., S.C., G.V., S.V., R.V., F.C., A.C.F., V.B., D.M., S.N., F.G., F.L., M.B., L.C., D.C.; laboratory analyses, L.M., M.A.F., V.V., D.M., F.G., G.P., S.N., G.I., Fl.G.,M.R.; field measurements, L.D.L, M.B., M.Ri., M.P., I.P., G.Ca., L.D.L., G.V., S.V., F.C., A.C.F., L.M., M.A.F., A.M., F.G.; toxicological, E.C., M.G., G.M., E.N., M.I., E.M., M.Ba., F.D.R., T.L.T., E.P., M.S., G.Z.; OP assays, M.Ri., M.R., L.M., M.A.F., S.C., G.D.I.; data analyses, F.Co, M.Ri., M.P., I.P., G.D.I., M.G., S.V., G.V., F.C., A.C.F., R.V., G.M., E.C., E.M., M.Ba., D.M., S.N.; data curation, F.Co., M.Ri., M.B, L.D.L.; writing—original draft preparation, F.Co., R.V.; writing—review and editing, F.Co., R.V., S.D., G.C., L.M., M.G., M.Ri., S.A., E.C., M.B., F.L., M.G.; project administration, S.D., F.Co., R.V.; funding acquisition, M.C.F., S.D., R.V., F.L., G.C., D.M. All authors have read and agreed to the published version of the manuscript."

Funding: This research was funded by Italian Ministry of the University (MIUR), grant number 2017MSN7M8

Data Availability Statement: The datasets used and/or analysed during the current study are available from the corresponding author on reasonable request.

Conflicts of Interest: "The authors declare no conflict of interest."

REFERENCES

1. World Health Organization, & WHO European Centre for Environment. (2021). WHO global air quality guidelines: particulate matter (PM2. 5 and PM10), ozone, nitrogen dioxide, sulfur dioxide and carbon monoxide. World Health Organization.
2. Cohen, A. J., Brauer, M., Burnett, R., Anderson, H. R., Frostad, J., Estep, K., ... & Forouzanfar, M. H. (2017). Estimates and 25-year trends of the global burden of disease attributable to ambient air pollution: an analysis of data from the Global Burden of Diseases Study 2015. *The Lancet*, *389*(10082), 1907-1918.
3. Chen, J., & Hoek, G. (2020). Long-term exposure to PM and all-cause and cause-specific mortality: a systematic review and meta-analysis. *Environment international*, *143*, 105974.
4. Stafoggia, M., Oftedal, B., Chen, J., Rodopoulou, S., Renzi, M., Atkinson, R. W., ... & Janssen, N. A. (2022). Long-term exposure to low ambient air pollution concentrations and mortality among 28 million people: results from seven large European cohorts within the ELAPSE project. *The Lancet Planetary Health*, *6*(1), e9-e18.
5. Li, X., Jin, L., & Kan, H. (2019). Air pollution: a global problem needs local fixes. Nature 2019 Jun;570(7762):437-439. doi: 10.1038/d41586-019-01960-7
6. EPA, D. (2009). Integrated science assessment for particulate matter. *US Environmental Protection Agency Washington, DC*.
7. World Health Organization. (2013). *Review of evidence on health aspects of air pollution: REVIHAAP project: technical report* (No. WHO/EURO: 2013-2663-42419-58845). World Health Organization. Regional Office for Europe.
8. Künzi, L., Krapf, M., Daher, N., Dommen, J., Jeannet, N., Schneider, S., ... & Geiser, M. (2015). Toxicity of aged gasoline exhaust particles to normal and diseased airway epithelia. *Scientific reports*, *5*(1), 1-10.

9. Jimenez, J. L., Canagaratna, M. R., Donahue, N. M., Prevot, A. S. H., Zhang, Q., Kroll, J. H., ... & Worsnop, D. R. (2009). Evolution of organic aerosols in the atmosphere. *Science*, *326*(5959), 1525-1529.
10. Ervens, B. T. B. W. R., Turpin, B. J., & Weber, R. J. (2011). Secondary organic aerosol formation in cloud droplets and aqueous particles (aqSOA): a review of laboratory, field and model studies. *Atmospheric Chemistry and Physics*, *11*(21), 11069-11102.
11. Corsini, E., Ozgen, S., Papale, A., Galbiati, V., Lonati, G., Fermo, P., ... & Marinovich, M. (2017a). Insights on wood combustion generated proinflammatory ultrafine particles (UFP). *Toxicology Letters*, *266*, 74-84.
12. Corsini, E., Vecchi, R., Marabini, L., Fermo, P., Becagli, S., Bernardoni, V., ... & Marinovich, M. (2017b). The chemical composition of ultrafine particles and associated biological effects at an alpine town impacted by wood burning. *Science of the Total Environment*, *587*, 223-231.
13. Marabini, L., Ozgen, S., Turacchi, S., Aminti, S., Arnaboldi, F., Lonati, G., ... & Marinovich, M. (2017). Ultrafine particles (UFPs) from domestic wood stoves: genotoxicity in human lung carcinoma A549 cells. *Mutation Research/Genetic Toxicology and Environmental Mutagenesis*, *820*, 39-46.
14. Costabile, F., Alas, H., Aufderheide, M., Avino, P., Amato, F., Argentini, S., ... & Gobbi, G. P. (2017). First results of the "Carbonaceous aerosol in Rome and Environs (CARE)" experiment: Beyond current standards for PM10. *Atmosphere*, *8*(12), 249.
15. Gualtieri, M., Grollino, M. G., Consales, C., Costabile, F., Manigrasso, M., Avino, P., ... & Zanini, G. (2018). Is it the time to study air pollution effects under environmental conditions? A case study to support the shift of in vitro toxicology from the bench to the field. *Chemosphere*, *207*, 552-564.
16. Kelly, F. J., & Fussell, J. C. (2012). Size, source and chemical composition as determinants of toxicity attributable to ambient particulate matter. *Atmospheric environment*, *60*, 504-526.
17. Lakey, P. S., Berkemeier, T., Tong, H., Arangio, A. M., Lucas, K., Pöschl, U., & Shiraiwa, M. (2016). Chemical exposure-response relationship between air pollutants and reactive oxygen species in the human respiratory tract. *Scientific reports*, *6*(1), 1-6.
18. Saffari, A., Daher, N., Shafer, M. M., Schauer, J. J., & Sioutas, C. (2014). Global perspective on the oxidative potential of airborne particulate matter: a synthesis of research findings. *Environmental science & technology*, *48*(13), 7576-7583.
19. Decesari, S., Sowlat, M. H., Hasheminassab, S., Sandrini, S., Gilardoni, S., Facchini, M. C., ... & Sioutas, C. (2017). Enhanced toxicity of aerosol in fog conditions in the Po Valley, Italy. *Atmospheric Chemistry and Physics*, *17*(12), 7721-7731.
20. Limón-Pacheco, J., & Gonsebatt, M. E. (2009). The role of antioxidants and antioxidant-related enzymes in protective responses to environmentally induced oxidative stress. *Mutation Research/Genetic Toxicology and Environmental Mutagenesis*, *674*(1-2), 137-147.
21. Ayres, J. G., Borm, P., Cassee, F. R., Castranova, V., Donaldson, K., Ghio, A., ... & Froines, J. (2008). Evaluating the toxicity of airborne particulate matter and nanoparticles by measuring oxidative stress potential—a workshop report and consensus statement. *Inhalation toxicology*, *20*(1), 75-99.
22. Verma, V., Fang, T., Xu, L., Peltier, R. E., Russell, A. G., Ng, N. L., & Weber, R. J. (2015). Organic aerosols associated with the generation of reactive oxygen species (ROS) by water-soluble PM2. 5. *Environmental science & technology*, *49*(7), 4646-4656.
23. Borm, P. J., Kelly, F., Künzli, N., Schins, R. P., & Donaldson, K. (2007). Oxidant generation by particulate matter: from biologically effective dose to a promising, novel metric. *Occupational and environmental medicine*, *64*(2), 73-74.
24. Janssen, N. A., Yang, A., Strak, M., Steenhof, M., Hellack, B., Gerlofs-Nijland, M. E., ... & Cassee, F. (2014). Oxidative potential of particulate matter collected at sites with different source characteristics. *Science of the Total Environment*, *472*, 572-581.
25. Sarti, E., Pasti, L., Rossi, M., Ascanelli, M., PAgnoni, A., Trombini, M., & Remelli, M. (2015). The composition of PM1 and PM2.5 samples, metals and their water soluble fractions in the Bologna area (Italy). *Atmospheric Pollution Research*,6, 708-718.
26. Vecchi, R., Marcazzan, G., Valli, G., Ceriani, M., Antoniazzi, C. (2004). The role of atmospheric dispersion in the seasonal variation of PM1 and PM2.5 concentration and composition in the urban area of Milan (Italy). *Atmospheric Environment*, 38, 4437–4446.
27. Amato, F., Alastuey, A., Karanasiou, A., Lucarelli, F., Nava, S., Calzolai, G., ... & Querol, X. (2016). AIRUSE-LIFE+: a harmonized PM speciation and source apportionment in five southern European cities. *Atmospheric Chemistry and Physics*, *16*(5), 3289-3309.
28. Gilardoni, S., Massoli, P., Paglione, M., Giulianelli, L., Carbone, C., Rinaldi, M., ... & Facchini, M. C. (2016). Direct observation of aqueous secondary organic aerosol from biomass-burning emissions. *Proceedings of the National Academy of Sciences*, *113*(36), 10013-10018.
29. Ricciardelli, I., Bacco, D., Rinaldi, M., Bonafè, G., Scotto, F., Trentini, A., ... & Poluzzi, V. (2017). A three-year investigation of daily PM2. 5 main chemical components in four sites: the routine measurement program of the Supersito Project (Po Valley, Italy). *Atmospheric Environment*, *152*, 418-430.
30. Lucarelli, F., Calzolai, G., Chiari, M., Giardi, F., Czelusniak, C., & Nava, S. (2020). Hourly elemental composition and source identification by Positive Matrix Factorization (PMF) of fine and coarse particulate matter in the high polluted industrial area of Taranto (Italy). *Atmosphere*, *11*(4), 419.
31. Massimi, L., Ristorini, M., Astolfi, M. L., Perrino, C., & Canepari, S. (2020a). High resolution spatial mapping of element concentrations in PM10: A powerful tool for localization of emission sources. *Atmospheric Research*, *244*, 105060.
32. Astolfi, M. L., Protano, C., Marconi, E., Massimi, L., Brunori, M., Piamonti, D., ... & Canepari, S. (2020). A new rapid treatment of human hair for elemental determination by inductively coupled mass spectrometry. *Analytical Methods*, *12*(14), 1906-1918.

33. Canepari, S., Pietrodangelo, A., Perrino, C., Astolfi, M. L., & Marzo, M. L. (2009). Enhancement of source traceability of atmospheric PM by elemental chemical fractionation. *Atmospheric Environment*, *43*(31), 4754-4765.
34. Piazzalunga, A., Bernardoni, V., Fermo, P., & Vecchi, R. (2013). Optimisation of analytical procedures for the quantification of ionic and carbonaceous fractions in the atmospheric aerosol and applications to ambient samples. *Analytical and bioanalytical chemistry*, *405*(2), 1123-1132.
35. Piazzalunga, A., Fermo, P., Bernardoni, V., Vecchi, R., Valli, G., & De Gregorio, M. A. (2010). A simplified method for levoglucosan quantification in wintertime atmospheric particulate matter by high performance anion-exchange chromatography coupled with pulsed amperometric detection. *International Journal of Environmental and Analytical Chemistry*, *90*(12), 934-947.
36. Terzopoulou, E., Voutsa, D., & Kaklamanos, G. (2015). A multi-residue method for determination of 70 organic micropollutants in surface waters by solid-phase extraction followed by gas chromatography coupled to tandem mass spectrometry. *Environmental Science and Pollution Research*, *22*(2), 1095-1112.
37. Gosetti, F., Chiuminatto, U., Mazzucco, E., Robotti, E., Calabrese, G., Gennaro, M. C., & Marengo, E. (2011). Simultaneous determination of thirteen polycyclic aromatic hydrocarbons and twelve aldehydes in cooked food by an automated on-line solid phase extraction ultra high performance liquid chromatography tandem mass spectrometry. *Journal of Chromatography A*, *1218*(37), 6308-6318.
38. Canagaratna, M. R., Jayne, J. T., Jimenez, J. L., Allan, J. D., Alfarra, M. R., Zhang, Q., ... & Worsnop, D. R. (2007). Chemical and microphysical characterization of ambient aerosols with the aerodyne aerosol mass spectrometer. *Mass spectrometry reviews*, *26*(2), 185-222.
39. Jayne, J. T., Leard, D. C., Zhang, X., Davidovits, P., Smith, K. A., Kolb, C. E., & Worsnop, D. R. (2000). Development of an aerosol mass spectrometer for size and composition analysis of submicron particles. *Aerosol Science & Technology*, *33*(1-2), 49-70.
40. Jimenez, J. L., Jayne, J. T., Shi, Q., Kolb, C. E., Worsnop, D. R., Yourshaw, I., ... & Davidovits, P. (2003). Ambient aerosol sampling using the aerodyne aerosol mass spectrometer. *Journal of Geophysical Research: Atmospheres*, *108*(D7).
41. DeCarlo, P. F., Kimmel, J. R., Trimborn, A., Northway, M. J., Jayne, J. T., Aiken, A. C., ... & Jimenez, J. L. (2006). Field-deployable, high-resolution, time-of-flight aerosol mass spectrometer. *Analytical chemistry*, *78*(24), 8281-8289.
42. Calzolai, G., Lucarelli, F., Chiari, M., Nava, S., Giannoni, M., Carrarese, L., Prati, P., & Vecchi, R. (2015). Improvements in PIXE analysis of hourly particulate matter samples. *Nuclear Instruments and Methods in Physics Research B*, 363, 99–104
43. Hinds, W.C. Aerosol technology: properties, behavior, and measurement of airborne particles. John Wiley & Sons. , 2nd ed.; Wiley: New York, NY, USA, 1999.
44. Massabò, D., Bernardoni, V., Bove, M. C., Brunengo, A., Cuccia, E., Piazzalunga, A., ... & Vecchi, R. (2013). A multi-wavelength optical set-up for the characterization of carbonaceous particulate matter. *Journal of Aerosol Science*, *60*, 34-46.
45. Massabò, D., Caponi, L., Bernardoni, V., Bove, M. C., Brotto, P., Calzolai, G., ... & Prati, P. (2015). Multi-wavelength optical determination of black and brown carbon in atmospheric aerosols. *Atmospheric Environment*, *108*, 1-12.
46. Moosmüller, H., Chakrabarty, R. K., Ehlers, K. M., & Arnott, W. P. (2011). Absorption Ångström coefficient, brown carbon, and aerosols: basic concepts, bulk matter, and spherical particles. *Atmospheric Chemistry and Physics*, *11*(3), 1217-1225.
47. Sandradewi, J., Prévôt, A. S., Szidat, S., Perron, N., Alfarra, M. R., Lanz, V. A., ... & Baltensperger, U. R. S. (2008). Using aerosol light absorption measurements for the quantitative determination of wood burning and traffic emission contributions to particulate matter. *Environmental science & technology*, *42*(9), 3316-3323.
48. Bernardoni, V., Pileci, R. E., Caponi, L., & Massabò D. (2017). The Multi-Wavelength Absorption Analyzer (MWAA) Model as a Tool for Source and Component Apportionment Based on Aerosol Absorption Properties: Application to Samples Collected in Different Environments. *Atmosphere*, 8(11), 218.
49. Massabò, D., Altomari, A., Vernocchi, V., & Prati, P. (2019). Two-wavelength thermal–optical determination of light-absorbing carbon in atmospheric aerosols. *Atmospheric Measurement Techniques*, *12*(6), 3173-3182.
50. Massabò, D., Prati, P., Canepa, E., Bastianini, M., Van Eijk, A. M., Missamou, T., & Piazzola, J. (2020). Characterization of carbonaceous aerosols over the Northern Adriatic Sea in the JERICO-NEXT project framework. *Atmospheric Environment*, *228*, 117449.
51. Drinovec, L., Močnik, G., Zotter, P., Prévôt, A. S. H., Ruckstuhl, C., Coz, E., ... & Hansen, A. D. A. (2015). The" dual-spot" Aethalometer: an improved measurement of aerosol black carbon with real-time loading compensation. *Atmospheric measurement techniques*, *8*(5), 1965-1979.
52. NIOSH: Method 5040 Issue 3: Elemental Carbon (Diesel Exhaust). In NIOSH Manual of Analytical Methods. National Institute of Occupational Safety and Health, Cincinnati, OH, 1999.
53. Frezzini, M. A., Castellani, F., De Francesco, N., Ristorini, M., Canepari, S. 2019. Application of DPPH assay for assessment of particulate matter reducing properties. Atmosphere, 10(12), 816.
54. Frezzini, M. A., De Francesco, N., Massimi, L., Canepari, S. 2021. Effects of operating conditions on PM oxidative potential assays. Atmospheric Environment, 118802.
55. Massimi, L., Ristorini, M., Simonetti, G., Frezzini, M. A., Astolfi, M. L., Canepari, S., 2020b. Spatial Mapping and Size Distribution of Oxidative Potential of Particulate Matter Released by Spatially Disaggregated Sources. Environmental Pollution, 115271.
56. Cho, A. K., Sioutas, C., Miguel, A. H., Kumagai, Y., Schmitz, D. A., Singh, M., ... & Froines, J. R. (2005). Redox activity of airborne particulate matter at different sites in the Los Angeles Basin. *Environmental research*, *99*(1), 40-47.

57. Verma, V., Ning, Z., Cho, A. K., Schauer, J. J., Shafer, M. M., & Sioutas, C. (2009). Redox activity of urban quasi-ultrafine particles from primary and secondary sources. *Atmospheric Environment*, *43*(40), 6360-6368.
58. Gao, D., Fang, T., Verma, V., Zeng, L., & Weber, R. J. (2017). A method for measuring total aerosol oxidative potential (OP) with the dithiothreitol (DTT) assay and comparisons between an urban and roadside site of water-soluble and total OP. *Atmospheric Measurement Techniques*, *10*(8), 2821-2835.
59. Simonetti, G., Frasca, D., Marcoccia, M., Farao, C., & Canepari, S. (2018a). Multi-elemental analysis of particulate matter samples collected by a particle-into-liquid sampler. *Atmospheric Pollution Research*, *9*(4), 747-754.
60. Costabile, F., Gualtieri, M., Canepari, S., Tranfo, G., Consales, C., Grollino, M. G., ... & Simonetti, G. (2019). Evidence of association between aerosol properties and in-vitro cellular oxidative response to PM1, oxidative potential of PM2. 5, a biomarker of RNA oxidation, and its dependency on combustion sources. *Atmospheric environment*, *213*, 444-455.
61. Corsini, E., Budello, S., Marabini, L., Galbiati, V., Piazzalunga, A., Barbieri, P., ... & Galli, C. L. (2013). Comparison of wood smoke PM2. 5 obtained from the combustion of FIR and beech pellets on inflammation and DNA damage in A549 and THP-1 human cell lines. *Archives of toxicology*, *87*(12), 2187-2199.
62. Battistoni, M., Bacchetta, R., Di Renzo, F., Metruccio, F., Moretto, A., & Menegola, E. (2022). Modified Xenopus laevis approach (R-FETAX) as an alternative test for the evaluation of foetal valproate spectrum disorder. *Reproductive Toxicology*, *107*, 140-149.
63. Brown, N. A., & Fabro, S. (1981). Quantitation of rat embryonic development in vitro: a morphological scoring system. *Teratology*, *24*(1), 65-78.
64. Nieuwkoop, P. D., Faber, J., Gerhart, J., & Kirschner, M. (2020). Normal table of Xenopus laevis (Daudin): a systematical and chronological survey of the development from the fertilized egg till the end of metamorphosis. Garland Science.
65. Massabò, D., Danelli, S. G., Brotto, P., Comite, A., Costa, C., Di Cesare, A., ... & Prati, P. (2018). ChAMBRe: a new atmospheric simulation chamber for aerosol modelling and bio-aerosol research. *Atmos. Meas. Tech.*, *11*(10), 5885-5900.
66. Danelli, S. G., Brunoldi, M., Massabò, D., Parodi, F., Vernocchi, V., & Prati, P. (2021). Comparative characterization of the performance of bio-aerosol nebulizers in connection with atmospheric simulation chambers. *Atmos. Meas. Tech.*, *14*(6), 4461-4470.
67. Vernocchi, V., Brunoldi, M., Danelli, S. G., Parodi, F., Prati, P., Massabò, D. (2021). Characterization of the MISG soot generator with an atmospheric simulation chamber. *Atmos. Meas. Tech.*, 15, 2159-2175.
68. Skamarock, W. C., Klemp, J. B., Dudhia, J., Gill, D. O., Barker, D. M., Wang, W., & Powers, J. G. (2005). *A description of the advanced research WRF version 2*. National Center For Atmospheric Research Boulder Co Mesoscale and Microscale Meteorology Div.
69. Falasca, S., & Curci, G. (2018). High-resolution air quality modeling: Sensitivity tests to horizontal resolution and urban canopy with WRF-CHIMERE. *Atmos. Environ.*, *187*, 241-254.
70. Menut, L., Bessagnet, B., Khvorostyanov, D., Beekmann, M., Blond, N., Colette, A., Coll, I., Curci, G., Foret, G., Hodzic, A., Mailler, S., Meleux, F., Monge, J.-L., Pison, I., Siour, G., Turquety, S., Valari, M., Vautard, R., & Vivanco, M. G. (2013). CHIMERE 2013: A model for regional atmospheric composition modelling. Geoscientific Model Development, 6(4), 981–1028. https://doi.org/10.5194/gmd-6-981-2013
71. Deserti, M., Bande, S., Angelino, E., Pession, G., Dalan, F., Minguzzi, M., Stortini, M., Bonafè, G., De Maria, R., Fossati, G., Peroni, E., Costa, M. P., Liguori, F., & Pillon, S. (2008). Rapporto tecnico sulla applicazione di modellistica al Bacino Padano Adriatico. Agenzia per la Protezione dell'Ambiente e per i servizi Tecnici (APAT) e Centro Tematico Nazionale – Atmosfera Clima ed Emissioni in Aria.
72. Costabile, F., Gilardoni, S., Barnaba, F., Di Ianni, A., Di Liberto, L., Dionisi, D., ... & Gobbi, G. P. (2017b). Characteristics of brown carbon in the urban Po Valley atmosphere. *Atmospheric Chemistry and Physics*, *17*(1), 313-326.
73. Simonetti, G., Conte, E., Perrino, C., & Canepari, S. (2018a). Oxidative potential of size-segregated PM in an urban and an industrial area of Italy. *Atmospheric Environment*, *187*, 292-300.
74. Manigrasso, M., Simonetti, G., Astolfi, M. L., Perrino, C., Canepari, S., Protano, C., ... & Vitali, M. (2019). Oxidative potential associated with urban aerosol deposited into the respiratory system and relevant elemental and ionic fraction contributions. *Atmosphere*, *11*(1), 6.
75. Molina, C., Toro A, R., Manzano, C. A., Canepari, S., Massimi, L., & Leiva-Guzmán, M. (2020). Airborne aerosols and human health: Leapfrogging from mass concentration to oxidative potential. *Atmosphere*, *11*(9), 917.
76. Verma, V., Sioutas, C., & Weber, R. J. (2018). Oxidative properties of ambient particulate matter-an assessment of the relative contributions from various aerosol components and their emission sources. In *Multiphase Environmental Chemistry in the Atmosphere* (pp. 389-416). American Chemical Society.
77. Bates, J. T., Fang, T., Verma, V., Zeng, L., Weber, R. J., Tolbert, P. E., ... & Russell, A. G. (2019). Review of acellular assays of ambient particulate matter oxidative potential: methods and relationships with composition, sources, and health effects. *Environmental science & technology*, *53*(8), 4003-4019.
78. Thurston, G., Chen, L., Campen, M.: Particle toxicity's role in air pollution. Science 375 (6580), 2022
79. Al-Kindi, S. G., Brook, R. D., Biswal, S., & Rajagopalan, S. (2020). Environmental determinants of cardiovascular disease: lessons learned from air pollution. *Nature Reviews Cardiology*, *17*(10), 656-672.
80. Chung, M. Y., Lazaro, R. A., Lim, D., Jackson, J., Lyon, J., Rendulic, D., & Hasson, A. S. (2006). Aerosol-borne quinones and reactive oxygen species generation by particulate matter extracts. *Environmental science & technology*, *40*(16), 4880-4886.

 doi:10.20944/preprints202204.0107.v1

81. Zhou, L., Hopke, P. K., Paatero, P., Ondov, J. M., Pancras, J. P., Pekney, N. J., & Davidson, C. I. (2004). Advanced factor analysis for multiple time resolution aerosol composition data. *Atmospheric Environment*, *38*(29), 4909-4920.
82. Ogulei, D., Hopke, P. K., Zhou, L., Paatero, P., Park, S. S., & Ondov, J. M. (2005). Receptor modeling for multiple time resolved species: the Baltimore supersite. *Atmospheric Environment*, *39*(20), 3751-3762.
83. Forello, A. C., Bernardoni, V., Calzolai, G., Lucarelli, F., Massabò, D., Nava, S., …, & Vecchi, R. (2019). Exploiting multi-wavelength aerosol absorption coefficients in a multi-time resolution source apportionment study to retrieve source-dependent absorption parameters. *Atmospheric Chemistry and Physics*, 19, 11235–11252.
84. Forello, A.C., Amato, F., Bernardoni, V., Calzolai, G., Canepari, S., Costabile, F., …, & Vecchi, R. (2020). Gaining knowledge on source contribution to aerosol optical absorption properties and organics by receptor modelling. *Atmospheric Environment*, 243, 117873